Evolution of the Coulomb interactions in correlated transition-metal perovskite oxides from the constrained random phase approximation

Liang Si [1,2,3,*] Peitao Liu [4,†] and Cesare Franchini [3,5,‡]

[1]School of Physics, Northwest University, Xi'an 710127, China
[2]Shaanxi Key Laboratory for Theoretical Physics Frontiers, Xi'an 710127, China
[3]Faculty of Physics and Center for Computational Materials Science, University of Vienna, Kolingasse 14-16, A-1090 Vienna, Austria
[4]Shenyang National Laboratory for Materials Science, Institute of Metal Research, Chinese Academy of Sciences, 110016 Shenyang, Liaoning, China
[5]Dipartimento di Fisica e Astronomia, Università di Bologna, Bologna 40126, Italy

(Received 31 July 2024; accepted 3 January 2025; published 23 January 2025)

Determining the strength of electronic correlations of correlated electrons plays important roles in accurately describing the electronic structures and physical properties of transition-metal (TM) perovskite oxides. Here, we study the evolution of electronic interaction parameters as a function of d-electron occupancy in an extended class of TM perovskite oxides ABO_3 (A = Sr, Ca, and $B = 3d$-$5d$ TM elements) using the constrained random-phase-approximation method adopting two distinct models: t_{2g}-t_{2g} and d-dp. For SrBO_3 with B = Fe, Ru, and Ir, the t_{2g}-t_{2g} model faces critical challenges, as the low-energy Hamiltonian spanning t_{2g} manifolds is ill-defined. The t_{2g}-t_{2g} model suggests that, for the early ABO_3 series ($B = d^1$–d^3), the bare Coulomb interaction parameters V remain nearly constant due to the competition between extended t_{2g} Wannier orbitals and bandwidth reduction. As the d-electron filling increases, both partially screened Coulomb interaction parameters U and fully screened Coulomb interaction parameters W decrease, which are attributed to enhanced e_g-t_{2g} and e_g-p screenings. In contrast to the t_{2g}-t_{2g} model, the d-dp model effectively handles both early and late ABO_3 perovskites and reveals different trends. Specifically, V varies inversely with the spreads of d orbitals. W reaches its minimum at the d^3 occupancy due to an interplay between increasing d-orbital localization and increasing screening effects. An unusual trend is observed for U, with local maxima at both d^1 and d^4 occupations. This can be understood from two aspects: (1) the increasing full screening effects from d^1 to d^3 and (2) the strongest d-d and the weakest d-p screening effects near d^4 for SrBO_3. Our results underscore that the Coulomb interaction parameters not only depend on the choice of model frameworks, but also the interplay between the localization of d orbitals and screening strength, which are affected by d-orbital fillings and details of the band dispersion.

DOI: 10.1103/PhysRevMaterials.9.015001

I. INTRODUCTION

The accurate simulations of material properties and phenomena through theoretical calculations rely heavily on understanding the intricate interactions between inhomogeneous distributed electrons. In many cases, these electronic interactions are governed by the crystal symmetry, lattices, and the constituent elements, making their precise determination challenging yet crucial for reliable theoretical predictions. For instance, after the experimental discovery and theoretical explanations for the Mott-insulator series [1,2], the scientific community has been convinced by the importance of the physics behind electronic correlation effects. For example, the Hubbard U explains the antiferromagnetic insulating state in transition-metal compounds [3], such as NiO [4,5], CeO_2 [6], Ce_2O_3 [7], CoO [8] and cuprate superconductor $CaCuO_2$ [9]. Additionally, the non-negligible U is found to be the driving force behind the Mott-insulating transition in V_2O_3 [10], and the orbital ordering state in cuprate $KCuF_3$ [11]. Another noteworthy case is the exotic insulating state in Sr_2IrO_4 due to the interplay between electronic correlation and spin-orbit interaction [12–14]. These observations demonstrate the significance of electronic correlation effects in oxides and their role in explaining emergent electronic and magnetic phases of matter.

Among the large family of oxide materials, transition-metal oxide (TMO) perovskites are an important class due to the intricate interplay between various degrees of freedom, including correlations, charge, spin, orbital, and lattice [15]. This complexity makes perovskite oxides a rich field of study for both experimental and theoretical research [16]. Electronic correlation effects in TMO perovskites are profound and impact virtually all their properties and potential functionalities. For strongly electronic correlated systems, such as solids that contain partially filled transition-metal or rare-earth elements, standard density-functional theory (DFT) often fails to account for electronic and magnetic properties. This necessitates the use of advanced beyond-DFT computational methods [17,18], such as DFT + U [8,9], dynamical mean-field theory (DMFT) [19,20], DFT + DMFT [21–23], dynamical vertex approximation (DΓA) [24,25] and

*Contact author: siliang@nwu.edu.cn
†Contact author: ptliu@imr.ac.cn
‡Contact author: cesare.franchini@univie.ac.at

GW + DMFT [26–32]. Theoretical research leveraging these advanced techniques has been pivotal in uncovering several exotic physical phenomena in perovskite oxides, including high-temperature superconductivity [33,34], colossal magnetoresistance [35–37], multiferroicity [38–42], topological electronic states [43,44] and exotic magnetic states [45–47]. Among all these correlated methods, the inclusion of a suitable Hubbard U is essential for obtaining a precise and materials specific description of the underlying physics.

However, accurately determining the electron interaction parameters is a nontrivial task. Physically, U corresponds to the difference between the electron affinity and the ionization energy when respectively adding and removing an electron on the correlated shell (e.g., the d shell) of a given atom, and in principle can be calculated from the experimental spectroscopy such as photoemission and inverse photoemission spectra [48]. Nevertheless, this requires the presence of a natural localized basis in the system, which does not apply for a majority of correlated materials due to the orbitals hybridization or spin-orbit coupling effects. The complexity of many-body interactions in solids often necessitates sophisticated theoretical frameworks and computational methodologies such as many-body perturbation theory [49] or quantum Monte Carlo simulations [50]. The fundamentally different formulation of the electronic structure problem in the DFT and lattice Hubbard model introduces complications when attempting to precisely define the parameters U and J for the DFT + + methods. The situation is further exacerbated by the adoption of different basis functions in commonly employed DFT codes and advanced many-body methods. In the past years, remarkable achievements have been made concerning the question of how to calculate U [51–55]. Most often, the U is taken as an adjustable parameter, which is obtained by fitting theoretical outputs with experimental spectra, e.g., x-ray photoemission and absorption spectra [56,57]. Within DFT, a common computational approach for obtaining U is the constrained DFT [also referred to as constrained local-density approximation (cLDA)] [51,52]. In this method, U^{cLDA} for a given shell is defined as the derivative of the total energy with respect to the variation of the electron occupancy. The cLDA method has been implemented within different basis functions and electronic-structure codes, e.g., in the (L)APW + lo framework [58] or in the basis of maximally localized Wannier functions [59], and applied to obtaining the U value for various materials [60–63].

An alternative widely adopted approach is the so-called constrained random phase approximation (cRPA), firstly proposed by Aryasetiawan *et al.* [64,65]. This method is based on the intuitive idea that the Hubbard U can be viewed as a Coulomb interaction screened by the polarization of the whole system excluding the polarization arising from a set of bands which are treated in the Hubbard model. For practical materials, the starting point is to downfold the full electronic structure of correlated systems to an effective low-energy Hamiltonian spanning by the correlated orbitals. Then, the Hubbard U and Hund's J for the effective low-energy Hamiltonian are defined as the matrix elements of the effective partially screened interactions, excluding the screenings from the correlated subspace. The cRPA method has been implemented in various codes such as WIEN2K [66], ABINIT [67], FLEUR [68], TOKYO *AB INITIO* program package [69], COULOMBU [70], spex [71], VASP [72], and quantum espresso [73]. The robust implementations therefore lead to wide applications of the cRPA method in computing the Hubbard U interactions for a variety of materials families, e.g., oxypnictides, parent compounds of Fe-based superconductors, and $3d$-$5d$ transition metals, $4f$ lanthanides, and their oxides [45,46,52,60,61,67,68,74–92].

Despite the numerous applications of the cRPA method, a comprehensive investigation on the evolution of electronic interaction parameters with the electron occupancy and bandwidth of the d shell of TM perovskite oxides across the entire range of TM elements is currently still lacking. In particular, the trends delivered by the widely adopted two schemes (i,e., t_{2g}-t_{2g} and d-dp) have not yet been carefully examined. The present work aims to fill in this gap by computing the bare Coulomb interaction parameters V, partially screened Coulomb interaction parameters U, and fully screened Coulomb interaction parameters W of a series of ABO_3 TM perovskite oxides (A = Sr and Ca, $B = 3d$ TMs from V to Co, $4d$ TMs from Nb to Rh, and $5d$ TMs from Ta to Pt). The resulting trends over the electron occupancy and bandwidth of the d shell within the t_{2g}-t_{2g} and d-dp approximations were revealed and discussed. This work underlines the significance of choosing an appropriate model and considering the counterbalanced effects between the localization of d orbitals and the strength of screenings in order to obtain a meaningful U value, and thus serves as an important addition to the community of correlated electrons.

II. METHOD AND COMPUTATIONAL DETAILS

A. Brief overview of the cRPA method

Initially, the cRPA method [65,74] was designed for calculating the Hubbard U value to merge DFT with DMFT [19,21,22,31,48,93,94]. In this regard, we formulate the cRPA starting from the model Hamiltonian

$$H = \sum_{\alpha\beta\mathbf{R}} t_{\alpha\beta}^{(\mathbf{R})} c_{\alpha\mathbf{R}}^{\dagger} c_{\beta\mathbf{R}} + \sum_{\alpha\beta\gamma\delta\mathbf{R}} U_{\alpha\beta\gamma\delta} c_{\alpha\mathbf{R}}^{\dagger} c_{\beta\mathbf{R}}^{\dagger} c_{\delta\mathbf{R}} c_{\gamma\mathbf{R}}, \quad (1)$$

where $t_{\alpha\beta}^{(\mathbf{R})}$ describes the electron hopping from the Wannier orbital $|w_\alpha\rangle$ to orbital $|w_\beta\rangle$ at the lattice vector $\mathbf{R}$. These hopping matrix elements can be obtained from Wannier interpolation of the Kohn-Sham eigenvalues $\epsilon_{n\mathbf{k}}$ [48]. $U_{\alpha\beta\gamma\delta}$ describes the effective on-site interaction between two particles and can be expressed as the expectation value of the partially screened Coulomb kernel $\mathcal{U}$ [66,95]:

$$\begin{aligned} U_{\alpha\beta\gamma\delta} &= \lim_{\omega\to 0} \langle w_\alpha, w_\beta | \mathcal{U}(\mathbf{r}, \mathbf{r}', \omega) | w_\delta, w_\gamma \rangle \\ &= \lim_{\omega\to 0} \iint d\mathbf{r}\, d\mathbf{r}' w_\alpha^*(\mathbf{r}) w_\beta^*(\mathbf{r}') \mathcal{U}(\mathbf{r}, \mathbf{r}', \omega) w_\delta(\mathbf{r}) w_\gamma(\mathbf{r}'). \end{aligned} \quad (2)$$

Within the framework of the cRPA, $\mathcal{U}$ is calculated via the RPA but using a "constrained" polarizability, i.e., the rest polarizability χ^r [65,74]

$$\mathcal{U} = \mathcal{V} + \mathcal{V}\chi^r\mathcal{U} \Leftrightarrow \mathcal{U}^{-1} = \mathcal{V}^{-1} - \chi^r. \quad (3)$$

Here, $\mathcal{V}$ is the bare Coulomb kernel. The rest polarizability χ^r contains all the RPA polarization effects except those within the correlated space [65,74]

$$\chi^r = \chi - \chi^c, \tag{4}$$

where χ is the total independent-particle polarizability at the RPA level [96–100] and χ^c is the correlated polarizability that contains the polarization effects within the correlated space only. The removal of χ^c from χ is to avoid double counting, since the polarization effects between the correlated electrons have already been accounted for by the many-body methods such as DMFT [32], thereby recovering the fully screened interaction $\mathcal{W}$ by

$$\mathcal{W} = \mathcal{U} + \mathcal{U}\chi^c\mathcal{W} \Leftrightarrow \mathcal{W}^{-1} = \mathcal{U}^{-1} - \chi^c. \tag{5}$$

B. Practical implementation of the cRPA method

As introduced above, the key part of the cRPA method is to remove the contribution of the correlated states from the total polarizability when calculating the partially screened Coulomb kernel. Such removal can be straightforwardly conducted either in the plane-wave basis [74] or in the Wannier function basis [69,101], if the correlated states form an isolated manifold around the Fermi level. However, when the correlated states are entangled with those noncorrelated (usually s or p) states of the system, the correlated space becomes not trivially defined and therefore the evaluation of χ^c has to be treated with care.

To address this problem, several methods have been proposed. Miyake *et al.* [75] proposed the disentanglement method. In this method, the correlated space C is disentangled from the full Fock space by diagonalizing the Hamiltonian in C and the remaining Fock space separately. This yields a minimal basis set within a given energy window that spans only the correlated space. The correlated polarizability is then obtained using the disentangled band structures based on the Adler and Wiser formula [102,103]. It is worth noting that the disentanglement method suffers from the deficiencies that it alters the band structure and the minimal basis set as well as the resulting U depend strongly on the chosen energy window of the Wannier functions [75].

To weaken the drawback of the disentanglement method, Şaşıoğlu *et al.* [68] proposed the weighted method. In this method, noncorrelated delocalized s and/or p states are included in the Wannier projection and the effective interaction is calculated using a weighted polarizability, where the weights are defined as probabilities for the Bloch states being correlated [67,68,70]. Although the weighted method does not change the band structure, it neglects the contributions to the polarizability from the nondiagonal terms of the correlated projectors [72].

A more consistent and elegant method for computing the correlated polarizability is the projector method, which was proposed by Kaltak [72] based on the Kubo-Nakano formula. This is also the method employed in the present work. In the following, we briefly summarize the key parts of this method. For more detailed deviations, we refer to Refs. [72,104]. Within the projector method, the correlated polarizability in reciprocal space is calculated as [72,102,103]

$$\begin{aligned}\chi^c_{\mathbf{G}\mathbf{G}'}(\mathbf{q},\omega) &= \frac{1}{N_\mathbf{k}}\sum_{\mathbf{k},n,n'}\frac{f_{n\mathbf{k}} - f_{n'\mathbf{k}-\mathbf{q}}}{\omega + \epsilon_{n\mathbf{k}} - \epsilon_{n'\mathbf{k}-\mathbf{q}} - \mathrm{i}\,\eta\,\mathrm{sgn}(\epsilon_{n\mathbf{k}} - \epsilon_{n'\mathbf{k}-\mathbf{q}})} \\ &\times \langle\bar{\psi}_{n\mathbf{k}}|e^{\mathrm{i}(\mathbf{q}+\mathbf{G})\mathbf{r}}|\bar{\psi}_{n'\mathbf{k}-\mathbf{q}}\rangle\langle\bar{\psi}_{n'\mathbf{k}-\mathbf{q}}|e^{-\mathrm{i}(\mathbf{q}+\mathbf{G}')\mathbf{r}'}|\bar{\psi}_{n\mathbf{k}}\rangle. \end{aligned}\tag{6}$$

Here, $\epsilon_{n\mathbf{k}}$ are the Kohn-Sham eigenvalues, $f_{n\mathbf{k}}$ are the occupancies, and η is a positive infinitesimal. $|\bar{\psi}_{n\mathbf{k}}\rangle$ is the projected Bloch function, which is defined as [72]

$$|\bar{\psi}_{n\mathbf{k}}\rangle = \sum_m P^{(\mathbf{k})}_{mn}|\psi_{m\mathbf{k}}\rangle, \tag{7}$$

where $|\psi_{n\mathbf{k}}\rangle$ are the Kohn-Sham eigenstates and $P^{(\mathbf{k})}_{mn}$ is the projection matrix with the correlated projector defined as [72]

$$\hat{P}^{(\mathbf{k})} = \sum_{\alpha\in C}|\Psi_{\alpha\mathbf{k}}\rangle\langle\Psi_{\alpha\mathbf{k}}|. \tag{8}$$

Here, the summation is restricted to the correlated space C and $|\Psi_{\alpha\mathbf{k}}\rangle$ is the mixed sate defined as [72]

$$|\Psi_{\alpha\mathbf{k}}\rangle = \sum_n T^{(\mathbf{k})}_{n\alpha}|\psi_{n\mathbf{k}}\rangle, \tag{9}$$

where $T^{(\mathbf{k})}_{n\alpha}$ is the unitary matrix used to project the Bloch functions to the Wannier functions and can be obtained from the wannier90 code [105–108]. Using Eqs. (8) and (9) one can obtain the compact form of the projection matrix as

$$P^{(\mathbf{k})}_{mn} = \langle\psi_{m\mathbf{k}}|\hat{P}^{(\mathbf{k})}|\psi_{n\mathbf{k}}\rangle = \sum_{\alpha\in C}T^{(\mathbf{k})}_{m\alpha}T^{*(\mathbf{k})}_{n\alpha}. \tag{10}$$

Having determined the correlated polarizability [Eq. (6)], the rest polarizability χ^r in reciprocal space is then obtained using Eq. (4) and the partially screened Coulomb kernel $\mathcal{U}_{\mathbf{G}\mathbf{G}'}(\mathbf{q},\omega)$ for every k point $\mathbf{q}$ in the irreducible wedge of the Brillouin zone is obtained using Eq. (3). Finally, the effective interaction matrix is evaluated via Eq. (2). After some mathematical derivations [72,104], the explicit effective interaction matrix is given by

$$\begin{aligned}U_{\alpha\beta\gamma\delta}(\omega) = \frac{1}{N_\mathbf{q}N^2_\mathbf{k}}\sum_{\mathbf{q},\mathbf{k},\mathbf{k}'}\sum_{\mathbf{G},\mathbf{G}'}\mathcal{U}_{\mathbf{G}\mathbf{G}'}(\mathbf{q},\omega)\langle\Psi_{\alpha\mathbf{k}}|e^{\mathrm{i}(\mathbf{q}+\mathbf{G})\mathbf{r}}|\Psi_{\delta\mathbf{k}-\mathbf{q}}\rangle \\ \times\langle\Psi_{\beta\mathbf{k}'-\mathbf{q}}|e^{-\mathrm{i}(\mathbf{q}+\mathbf{G}')\mathbf{r}'}|\Psi_{\gamma\mathbf{k}'}\rangle.\end{aligned}\tag{11}$$

In deriving the above formula, we have used the translation-invariant symmetry and Fourier transformation

$$\mathcal{U}(\mathbf{r},\mathbf{r}',\omega) = \frac{1}{N_\mathbf{q}}\sum_\mathbf{q}\sum_{\mathbf{G},\mathbf{G}'}e^{\mathrm{i}(\mathbf{q}+\mathbf{G})\mathbf{r}}\mathcal{U}_{\mathbf{G}\mathbf{G}'}(\mathbf{q},\omega)e^{-\mathrm{i}(\mathbf{q}+\mathbf{G}')\mathbf{r}'}, \tag{12}$$

as well as the definition of the Wannier functions

$$|w_\alpha\rangle \equiv |w_{\alpha\mathbf{R}}\rangle = \frac{1}{N_\mathbf{k}}\sum_\mathbf{k}e^{-\mathrm{i}\mathbf{k}\mathbf{R}}|\Psi_{\alpha\mathbf{k}}\rangle. \tag{13}$$

From the full effective interaction matrix [Eq. (11)] one can obtain the so-called Hubbard-Kanamori parameters (intraorbital interaction U, interorbital interaction U', and Hund's coupling J) [66,109] by

$$U = \frac{1}{N}\sum_{\alpha}^{N} U_{\alpha\alpha\alpha\alpha}(\omega = 0), \tag{14}$$

$$U' = \frac{1}{N(N-1)}\sum_{\alpha\neq\beta}^{N} U_{\alpha\beta\beta\alpha}(\omega = 0), \tag{15}$$

$$J = \frac{1}{N(N-1)}\sum_{\alpha\neq\beta}^{N} U_{\alpha\beta\alpha\beta}(\omega = 0). \tag{16}$$

Here, N is the number of correlated states that span the correlated space. Similarly, the bare and fully screened Coulomb interactions can be calculated as

$$V = \frac{1}{N}\sum_{\alpha}^{N} V_{\alpha\alpha\alpha\alpha}(\omega = 0), \tag{17}$$

$$W = \frac{1}{N}\sum_{\alpha}^{N} W_{\alpha\alpha\alpha\alpha}(\omega = 0), \tag{18}$$

where the matrix elements $V_{\alpha\beta\gamma\delta}$ and $W_{\alpha\beta\gamma\delta}$ are obtained using Eq. (11) but with $\mathcal{U}$ replaced with $\mathcal{V}$ and $\mathcal{W}$, respectively.

C. Computational details

First-principles DFT and cRPA calculations were conducted using the VASP code [110,111]. The exchange-correlation functional parametrized by Perdew, Burke, and Ernzerhof (PBE) was employed [112]. The energy cutoffs for the plane-wave basis set and the response function were set to 500 and 333 eV, respectively. Structural relaxation using the GGA-PBE exchange-correlation functional [112] often results in overestimated lattice constants and volumes. To address this, a modified version of PBE, known as PBE for solids, was proposed [113], which provides better agreement between theoretical relaxed lattices and experimental values. However, the slightly modified lattices result in negligible changes in the V, U, and J parameters. Therefore, we continue to use the standard PBE for relaxations and calculations. A Γ-centered k-point grid of $13 \times 13 \times 13$ was employed for sampling the Brillouin zone. The Gaussian smearing method with a smearing width of 0.05 eV was used. The lattice constants for all the ABO_3 compounds considered were optimized before performing the electronic structure, Wannier projections, and cRPA calculations. The convergence criteria for the electronic optimization and structural relaxation were set to 10^{-8} eV and 1 meV/Å, respectively. To construct the low-energy Hamiltonian and obtain the projection matrix, the maximally localized Wannier functions within the B-t_{2g} or B-d + O-$2p$ subspace were conducted using the WANNIER90 code [105–107]. The effective interaction matrix was calculated within the cRPA method using the projector method [72].

III. RESULTS AND DISCUSSION

A. DFT band structure

We start our discussion by presenting the band structures of ABO_3 perovskites. Since the trends over the d-electron filling of TM atoms are the main focus of our study, we limit ourselves to the (undistorted) cubic phase of ABO_3 perovskite TMOs. The cubic phase with $Pm3m$ space group was considered as the ground-state structure for some ABO_3 perovskites, such as 3d perovskite $SrVO_3$ [114] and $SrCrO_3$ [115], but not for some 4d and 5d ABO_3 compounds, such as $SrNbO_3$ [116], $SrRuO_3$ [117] and $SrIrO_3$ [118]. Here, we employ the cubic $Pm3m$ structure for all ABO_3 compounds to calculate the band structures and interaction parameters, as this simplification significantly reduces the computational efforts. With this setup, the TM cations in ABO_3 are octahedrally coordinated with O ligands, leading to band splittings between d orbitals into threefold degenerate t_{2g} and double degenerate e_g states. Compared with t_{2g} orbitals, the e_g orbitals host stronger d-p hybridization because their orbitals' lobes directly point to the O-p orbitals along the x, y, and z directions. The atomic number of the B site changes the interaction parameters by variation of the lattice constants and the d-band filling. Based on the relaxed lattice constants collected in Table I, the relaxed lattice in 3d-5d ABO_3 decreases as the atomic number of B increases. Hence, the d-band filling is expected to play a more important role. Additionally, as the d-band filling increases, the shift of Fermi energy leads to smaller energetic separation between the d band and the O-2p band, thereby further inducing strong d-p hybridization in addition to the lattice shrinking.

The DFT calculated nonmagnetic band structures of Sr-based 3d-5d ABO_3 are displayed in Figs. 1–3 (see Figs. 6–8 in the Appendix for the bands of Ca-based ABO_3), respectively. The DFT optimized lattice parameters are listed in Table I. One can see from Fig. 1 that as the d-band filling increases from $3d^1$ to $3d^5$, several distinct trends become apparent: (1) The t_{2g} bandwidths shrink, and their energies shift downward, coming into contact with O-2p bands from $3d^3$ ($SrMnO_3$) and $3d^4$ ($SrFeO_3$). (2) The e_g bands also shrink and shift to lower energies, making contact with t_{2g} bands starting from $3d^3$ ($SrMnO_3$). These factors lead to a significant reduction in the total d bandwidth with increasing d-band filling from d^1–d^5. (3) The O-2p bands, spanning from approximately -7.0 to -2.0 eV for $3d^1$ $SrVO_3$ and -7.0 to 0.0 eV for $3d^5$ $SrCoO_3$, shift upward towards the Fermi energy with band filling, eventually overlapping with d bands. (4) The Sr-d bands, initially above $\sim$4 eV, shift upward with increasing d-band filling. (5) For $3d^1$ $SrVO_3$ to $3d^3$ $SrMnO_3$, distinct and separated t_{2g} bands are obtained; however, for both $3d^4$ $SrFeO_3$ and $3d^5$ $SrCoO_3$, their t_{2g} bands undergo strong hybridization with O-2p bands, making the projection of DFT bands onto t_{2g}-based Wannier orbitals impractical.

As a consequence, when the B-site atomic number increases, the d orbitals undergo bandwidth reduction while the distance between the d and p bands decreases, leading to an enhancement in hybridization between d and p orbitals from early to late ABO_3. This trend is further supported by the decrease in the d-p charge transfer energy (Δ_{dp}), in qualitative agreement with optics experiments [119]. Additionally, the

TABLE I. DFT calculated lattice parameters that are used for cRPA calculations of cubic perovskites AMO_3 and energy window $\mathbb{W}$ for t_{2g}-t_{2g} and d-dp models. Both t_{2g} and d-dp Wannier functions are constructed out of the Kohn-Sham states included in $\mathbb{W}$. Because of the strong hybridization between late transition metals, e.g., Co, Rh, and Ir, no distinguishable t_{2g} bands can be projected onto local Wannier functions, and the t_{2g}-t_{2g} model is not considered for $ACoO_3$, $ARhO_3$, and $AIrO_3$ (A = Sr and Ca). Unit of energy window in eV.

	$SrMO_3$	a (Å)	$\mathbb{W}_{t_{2g}}$	$\mathbb{W}_{dp}$
$3d^1$	$SrVO_3$	3.862	[−0.98, 1.50]	[−7.18, 5.36]
$3d^2$	$SrCrO_3$	3.823	[−0.83, 1.53]	[−6.72, 5.36]
$3d^3$	$SrMnO_3$	3.803	[−1.50, 0.83]	[−7.12, 4.57]
$3d^4$	$SrFeO_3$	3.807	[−1.60, 0.58]	[−6.89, 4.13]
$3d^5$	$SrCoO_3$	3.815		[−6.80, 3.60]
$4d^1$	$SrNbO_3$	4.055	[−0.27, 3.56]	[−7.18, 9.03]
$4d^2$	$SrMoO_3$	4.014	[−0.98, 2.62]	[−7.29, 7.97]
$4d^3$	$SrTcO_3$	3.963	[−2.02, 1.53]	[−7.79, 7.99]
$4d^4$	$SrRuO_3$	3.953	[−2.69, 0.77]	[−7.89, 5.81]
$4d^5$	$SrRhO_3$	3.972		[−7.33, 5.11]
$5d^1$	$SrTaO_3$	4.062	[−1.35, 3.03]	[−9.32, 9.13]
$5d^2$	$SrWO_3$	4.013	[−2.18, 2.50]	[−9.90, 8.14]
$5d^3$	$SrReO_3$	3.978	[−2.65, 1.42]	[−9.66, 7.37]
$5d^4$	$SrOsO_3$	3.978	[−2.95, 1.00]	[−9.13, 7.49]
$5d^5$	$SrIrO_3$	3.987		[−8.73, 6.00]
$5d^6$	$SrPtO_3$	4.036		[−8.00, 5.21]
	$CaMO_3$	a (Å)	$\mathbb{W}_{t2g}$	$\mathbb{W}_{dp}$
$3d^1$	$CaVO_3$	3.805	[−1.02, 1.52]	[−7.44, 5.72]
$3d^2$	$CaCrO_3$	3.746	[−1.54, 0.93]	[−7.69, 5.18]
$3d^3$	$CaMnO_3$	3.724	[−1.80, 0.54]	[−7.65, 4.68]
$3d^4$	$CaFeO_3$	3.716	[−1.95, 0.32]	[−7.50, 4.33]
$3d^5$	$CaCoO_3$	3.732		[−7.14, 4.00]
$4d^1$	$CaNbO_3$	4.018	[−1.40, 2.79]	[−8.32, 8.52]
$4d^2$	$CaMoO_3$	3.954	[−2.00, 1.79]	[−8.66, 7.45]
$4d^3$	$CaTcO_3$	3.913	[−2.55, 1.11]	[−8.62, 6.73]
$4d^4$	$CaRuO_3$	3.900	[−2.84, 0.73]	[−8.24, 6.15]
$4d^5$	$CaRhO_3$	3.917		[−7.70, 5.46]
$5d^1$	$CaTaO_3$	4.026	[−1.45, 3.40]	[−9.43, 9.24]
$5d^2$	$CaWO_3$	3.966	[−2.41, 2.40]	[−9.90, 8.61]
$5d^3$	$CaReO_3$	3.938	[−2.75, 1.50]	[−9.83, 7.68]
$5d^4$	$CaOsO_3$	3.931	[−3.06, 1.00]	[−9.46, 7.00]
$5d^5$	$CaIrO_3$	3.941		[−9.03, 6.30]
$5d^6$	$CaPtO_3$	3.941		[−8.27, 5.57]

charge transfer energy is larger in $5d$ and $4d$ than in $3d$, which is attributed to the larger orbital extension of the former (compare Figs. 3 and 2 to Fig. 1).

B. d-dp approximation for Sr-based $3d$ series

The cRPA derived interaction parameters for the $3d$-$5d$ Sr-based ABO_3 series using the d-dp model are presented in Table II and Fig. 4.

We start from analyzing the tendencies of the interactions evolution with the atomic number in Sr-based $3d$ series. In Fig. 4, the d-dp interactions for the bare (V), partially (U), and fully screened (W) Coulomb interactions of $SrBO_3$ are shown. As band filling and atomic number increase within the same period of the periodic table ($3d$), the bare interactions V monotonously increase from 20.9 eV ($3d^1$ $SrVO_3$) to 26.2 eV ($3d^5$ $SrCoO_3$) [Fig. 4(a)]. The values obtained using the d-dp model are larger than the previous estimates based on the t_{2g}-t_{2g} approximation, such as 15.8 [120] and 16.1 eV [66] for $SrVO_3$, but are closer to the value derived from the d-dp model, which is, for instance, 19.5 eV for $SrVO_3$ using the (L)APW + lo framework in Ref. [66]. Additionally, the degree of orbital localization of d orbitals ($t_{2g} + e_g$ basis), which varies with the inverse of the Wannier d-orbital spreads, monotonously increases. Thus, the less extended the orbitals, the higher the bare Coulomb repulsion V. This means that the values of bare interactions are merely decided by the localization of correlated orbitals (i.e., the d orbitals for the d-dp model). Besides the Wannier orbital spreads, another measure of orbital localization is the bandwidth (Fig. 1, bottom panels). From $3d^1$ to $3d^5$, the d bands progressively approach the O-$2p$ bands, eventually overlapping at $3d^4$ $SrFeO_3$, which results in increased d-p hybridization. This leads to a noticeable reduction in d bandwidth, evident in both the band structures and density of states (DOS) plots (as shown in Figs. 1–3).

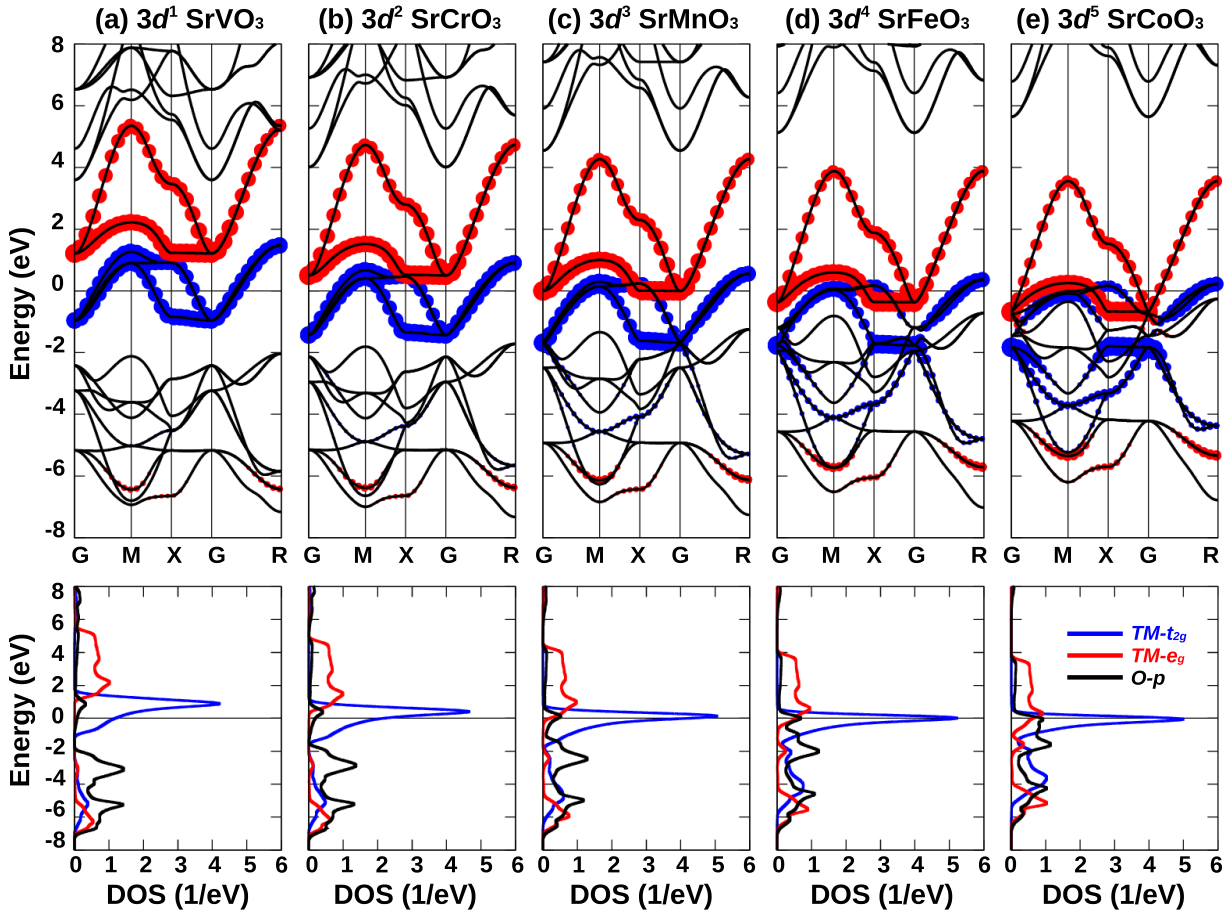

FIG. 1. DFT bands (top panels) and density of states (bottom panels) of SrBO$_3$ (B = V, Cr, Mn, Fe, and Co). The size of the blue and red points indicates contributions from t_{2g} and e_g orbitals.

Next, let us delve into the evolution of the fully screened interaction W. Unlike the bare interaction V, W accounts for electronic screening from all screening channels resulting from electronic polarization. Larger screening effects lead to stronger reduction from V to W. The values we obtained are highly consistent with previous reports for 3d SrBO$_3$ systems, such as SrVO$_3$, SrCrO$_3$, and SrMnO$_3$ [66], for which the W are in the region between 1.0 and 1.5 eV. Interestingly, W for the Sr-based 3d series initially decreases from 1.5 eV ($3d^1$ SrVO$_3$) to 1.2 eV ($3d^3$ SrMnO$_3$), then increases from $3d^3$ to $3d^5$ SrCoO$_3$ (1.3 eV), reaching a minimum at $3d^3$ SrMnO$_3$. This indicates a consequence of a significantly increased full screening from $3d^1$ to $3d^3$, counteracting the enhancement of orbital localization and bare V. However, from $3d^3$ to $3d^5$, the screening effect remains relatively constant.

The local minimum of W at $3d^3$ indicates a predominant influence of increasing screening effect from $3d^1$ to $3d^3$. This observation aligns with the reduction in bandwidth within the 3d series. In correlated systems, full electronic screening (mediating V to W) involves the creation of particle-hole and plasma excitation. At the RPA level, the strength of full screening is inversely proportional to the energy difference between occupied and unoccupied states. Examining the DFT bands in Figs. 1(a)–1(e), we observe a reduction in bandwidth as the d-electron number increases, causing the empty and occupied states to approach each other near the Fermi energy. The diminished separation between occupied and empty states leads to a stronger full screening effect, and consequently, a smaller W. This bandwidth reduction explains the decrease in W and the enhancement of full screening from $3d^1$ to $3d^3$. The increasing screening, in turn, counteracts the tendency towards more localized 3d orbitals and the enhancement of bare interaction V.

From $3d^3$ (SrMnO$_3$) to $3d^5$ (SrCoO$_3$), W increases from 1.15 to 1.29 eV. This can be understood from two aspects: (1) the bare interaction V already increases to a large value of 26.19 eV in $3d^5$, and even though the full screening in the localized 3d series is significant, it fails to counteract the effect of increasing localization; (2) as the atomic number and 3d-band filling increase, the unoccupied states gradually become occupied due to the shift of the Fermi energy. This decreases the possibility of creating particle-hole excitations around E_f, counteracting the enhancement of the full screening effect. To quantify the full screening strength in the 3d series, we calculated the ratio between W and V, as shown in Fig. 4(g) and Table II. We obtained values of 0.072, 0.055, 0.048, 0.046, and 0.049 from $3d^1$ SrVO$_3$ to $3d^5$ SrCoO$_3$, respectively. The tendency of W/V is basically consistent with that of W, indicating that W is mediated by full screening strength.

Before inspecting the trend of the partially screened Coulomb interaction U, we first classify the full screening

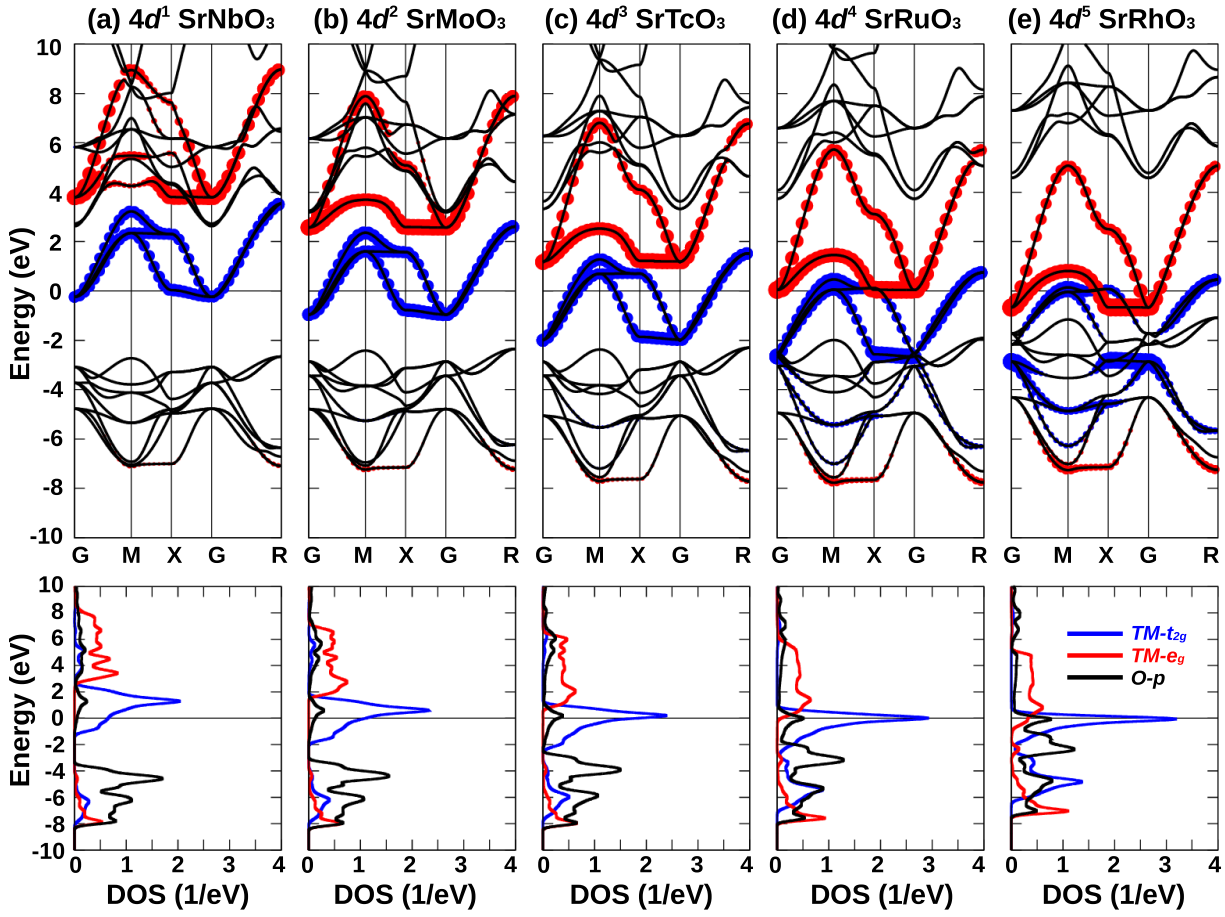

FIG. 2. DFT bands (top panels) and density of states (bottom panels) of SrBO_3 (B = Nb, Mo, Tc, Ru, and Rh). The size of the blue and red points indicates contributions from t_{2g} and e_g orbitals.

effect in the Sr-based ABO_3 series into three major contributions: (1) the d-d screening, i.e., the screening from occupied d-t_{2g} states to unoccupied t_{2g} and e_g states; (2) the d-p screening, i.e., the screening from occupied O-2p states to unoccupied d (mostly e_g in ABO_3) states; (3) the rest screening, which (mostly) consists of the screening from occupied d and O-2p states to the higher unoccupied Sr-4d states. After removing the d-d contribution from the full screening [which is the summation of (1)–(3)], the remaining partial screening consists of the (2) d-p and (3) rest screening. Unlike V and W, the partially screened interaction, i.e., the Hubbard U, exhibits an unusual tendency: two maximum values of U are found at $3d^1$ $SrVO_3$ and $3d^4$ $SrFeO_3$, respectively. To quantify the strength of partial screening, we also calculate the ratio between U and V, as shown in Fig. 4(d) and Table II.

From $3d^1$ to $3d^2$, U decreases from 3.25 to 2.64 eV. This reduction agrees with the tendency of W, indicating that d-p screening dominates the process from $3d^1$ to $3d^2$. A similar reduction in U from $SrVO_3$ to $SrCrO_3$, based on the $t_{2g} + p$ model, was previously observed in Ref. [66] and recently reported in Ref. [121]. Please note that for both $SrVO_3$ and $SrCrO_3$, the e_g bands are well separated from the t_{2g} bands [see Figs. 1(a) and 1(b)]. Therefore, including e_g bands in the model for cRPA calculations is not expected to significantly influence the resulting values. From $3d^2$ to $3d^3$, the U remains almost constant with a slight enhancement from 2.64 to 2.79 eV. The partial screening strength (U/V) for $3d^2$ and $3d^3$ is the same, indicated by U/V as 0.118 (Table II). This means that the summation of rest screening and d-p screening in $3d^2$ $SrCrO_3$ and $3d^3$ $SrMnO_3$ are comparable. However, the full screening strength in $3d^3$ is obviously stronger than that in $3d^2$ $SrCrO_3$ [Fig. 4(g) and Table II: W/U is 0.055 for $3d^2$ and 0.048 for $3d^3$]. Hence, we conclude that the d-d screening, excluded in the calculations for Hubbard U, is much stronger in $3d^3$ $SrMnO_3$ than in $3d^2$ $SrCrO_3$. This can be explained by their electronic structures [Figs. 1(b) and 1(c)]: in the bands of $SrCrO_3$ and $SrMnO_3$, the d bandwidth of $3d^3$ $SrMnO_3$ is obviously reduced compared with that of $3d^2$ $SrCrO_3$. This shortens the energetic distance between occupied and unoccupied d states, leading to an enhanced d-d screening. Moreover, as shown in the DOSs (bottom panels of Fig. 1), when one more electron is distributed to the t_{2g} orbital in $3d^3$ $SrMnO_3$, more t_{2g} states are occupied, increasing the possibility of forming particle-hole excitations in d orbitals. This explains the stronger d-d screening in $3d^3$ than in $3d^2$ and why there are comparable summations of d-p and rest screening in both $3d^2$ and $3d^3$. Considering that the bare V is 23.62 eV in $3d^3$ $SrMnO_3$ and 22.26 eV in $3d^2$ $SrCrO_3$, the Hubbard U in $SrMnO_3$ is slightly larger (0.149 eV) than in $SrCrO_3$.

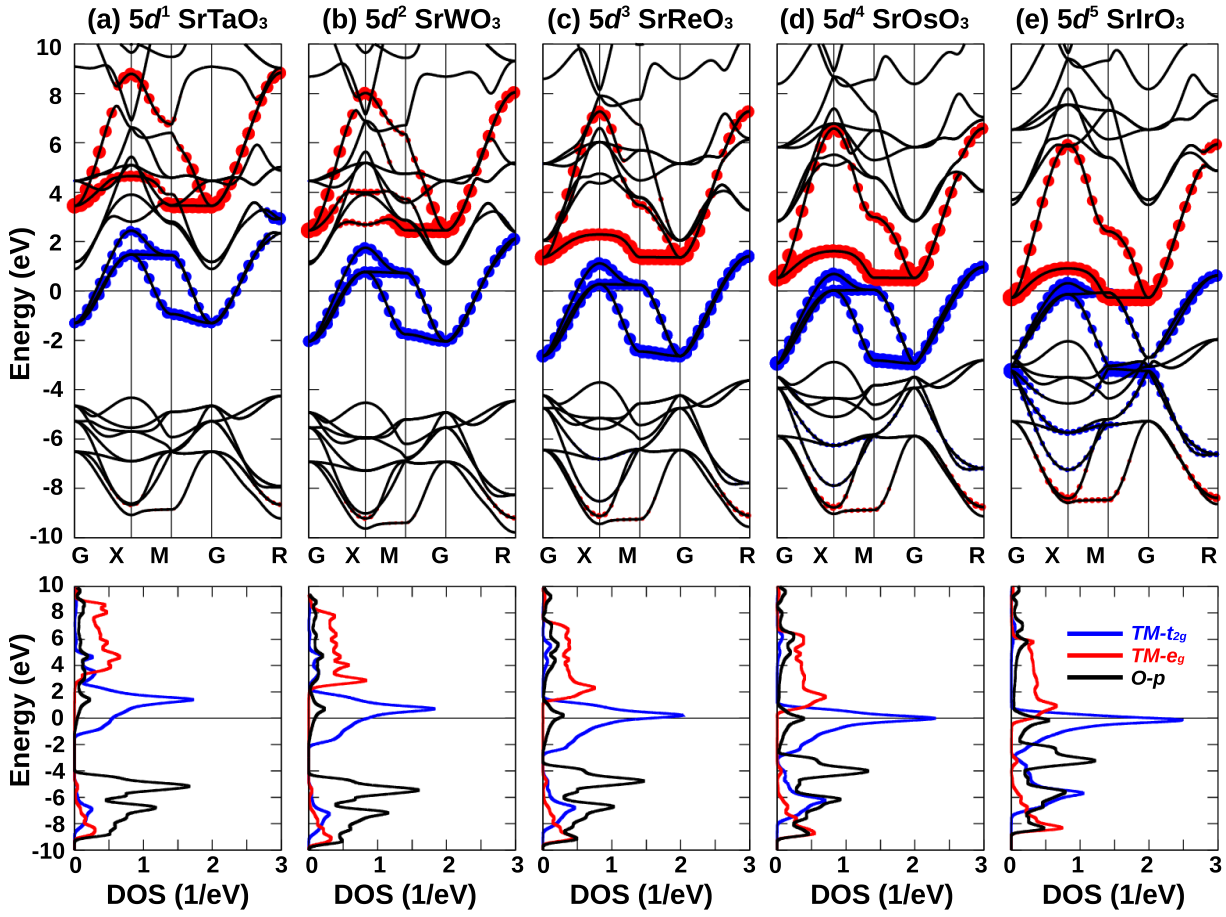

FIG. 3. DFT bands (top panels) and density of states (bottom panels) of SrBO$_3$ (B = Ta, W, Re, Os, and Ir). The size of the blue and red points indicates contributions from t_{2g} and e_g orbitals.

The transition from $3d^3$ SrMnO$_3$ to $3d^4$ SrFeO$_3$ exhibits an unusual behavior. The Hubbard U in $3d^4$ is 3.48 eV, approximately 0.69 eV larger than that of $3d^3$ SrMnO$_3$ (2.79 eV). This local maximum of U indicates that the summation of d-p and rest screening is significantly weaker in $3d^4$ than in $3d^3$. Moreover, the full screening strength (W/V) is stronger in $3d^4$ than in $3d^3$ (as shown in Table II: W/U is 0.046 for $3d^4$ and 0.048 for $3d^3$). Hence, the d-d screening in $3d^4$ represents a local maximum among the $3d$ series. This is explained by the DOSs in Fig. 1. For $3d^4$, both the t_{2g} and e_g states overlap around E_f, and the t_{2g} states are almost fully filled; the DOS peak is located at E_f (similar to $4d^4$ SrRuO$_3$). The number of occupied and unoccupied states is comparable (four electrons and six holes in d), resulting in a larger possibility of particle-hole excitation and d-d screening.

From $3d^4$ to $3d^5$ SrCoO$_3$, the Hubbard U drops to 2.70 eV, indicating that $3d^5$ exhibits the strongest partial screening strength (d-p plus the rest screening) among $3d^1$ to $3d^5$ and the corresponding weakest d-d screening. In $3d^5$, the d-p screening dominates the U, and the exclusion of d-d screening in d-dp approximation has a tiny influence on the physics and does not significantly differ U and W. This can be explained by the DOSs in Fig. 1(e). The O-2p states form three peaks in the entire energy region. For instance, in Fig. 1(a) showing the DOS of $3d^1$ SrVO$_3$, three O-2p peaks are found at approximately -5.5, -3.5, and 0.5 eV, respectively. The two lower O-2p peaks are formed by the O-2p bands, while the one near E_f is the hybridization peak with obvious V-$3d$ orbital characters. As the d electron increases, the hybridization peak gradually shifts down, while the O-2p peaks below E_f shift up. Approaching $3d^5$ SrCoO$_3$ [Fig. 1(e)], the upper O-2p peak approaches the hybridization peak and finally overlaps with it in $3d^5$ SrCoO$_3$, forming a higher O-2p peak near E_f. The d-p screening contribution is significantly enhanced by the formation of this peak, becoming the largest contribution instead of the d-d screening to the full screening. Even when d-d screening is excluded in the d-dp model, the remaining d-p screening still plays an effective role in reducing the V to a smaller U.

C. d-dp approximation for Sr-based 4d and 5d series

As shown in Figs. 4(b), 4(e), 4(h), and Table II, the trend of V, W, and U in the Sr-based 4d ABO$_3$ are roughly similar to those in the $3d$ ones. The bare V in 4d are generally smaller than those in $3d$, given the more extended nature of 4d orbitals, and our previous discussion confirms that the bare V is primarily determined by the degree of d-orbital localization.

The behaviors of Hubbard U in 4d ABO$_3$ are akin to those in $3d$ ones, with two maxima observed at $4d^1$ SrNbO$_3$ and

TABLE II. Bare V, Hubbard U, and fully screened W interactions, and corresponding Hund's exchange J_{bare}, J, and J_{screened} between d orbitals within d-dp approximation for $SrMO_3$ (M = V, Cr, Mn, Fe, Co, Nb, Mo, Tc, Ru, Rh, Ta, W, Re, Os, Ir, and Pt) perovskites. Their Wannier orbital spreads are also shown. All the energy units are in eV.

	d^1	d^2	d^3	d^4	d^5	d^6	d^1	d^2	d^3	d^4	d^5	d^6
$3d$	$SrVO_3$	$SrCrO_3$	$SrMnO_3$	$SrFeO_3$	$SrCoO_3$		$CaVO_3$	$CaCrO_3$	$CaMnO_3$	$CaFeO_3$	$CaCoO_3$	
U	3.24	2.64	2.79	3.48	2.70		3.42	2.85	2.85	4.88	2.84	
J	0.62	0.63	0.66	0.69	0.73		0.64	0.65	0.67	0.70	0.74	
V	20.88	22.25	23.62	24.91	26.19		21.09	22.54	23.67	25.00	26.28	
J_{bare}	0.74	0.76	0.80	0.84	0.88		0.75	0.77	0.80	0.84	0.88	
W	1.51	1.22	1.15	1.17	1.29		1.57	1.27	1.18	1.19	1.32	
J_{screened}	0.55	0.51	0.50	0.53	0.58		0.56	0.52	0.51	0.53	0.59	
U'	1.97	1.36	1.44	2.05	1.22		2.12	1.54	1.50	3.44	1.34	
U/V	15.5%	11.8%	11.8%	13.9%	10.3%		16.2%	12.6%	12.0%	19.5%	10.8%	
W/V	7.2%	5.5%	4.8%	4.6%	4.9%		7.4%	5.6%	4.9%	4.7%	5.0%	
Wannier spreads	3.34	3.06	2.69	2.41	2.19		3.10	2.75	2.72	2.40	2.17	
$4d$	$SrNbO_3$	$SrMoO_3$	$SrTcO_3$	$SrRuO_3$	$SrRhO_3$		$CaNbO_3$	$CaMoO_3$	$CaTcO_3$	$CaRuO_3$	$CaRhO_3$	
U	3.54	3.09	3.03	3.40	2.86		3.22	2.96	2.97	3.46	2.83	
J	0.46	0.49	0.52	0.53	0.54		0.47	0.50	0.52	0.54	0.54	
V	14.75	15.57	16.54	17.29	18.12		14.80	15.73	16.52	17.42	18.26	
J_{bare}	0.58	0.61	0.64	0.67	0.70		0.58	0.61	0.64	0.67	0.71	
W	1.59	1.20	1.13	1.16	1.59		1.63	1.25	1.14	1.18	1.41	
J_{screened}	0.42	0.41	0.40	0.40	0.43		0.43	0.42	0.41	0.41	0.43	
U'	2.58	2.08	1.97	2.29	1.71		2.27	1.94	1.92	2.34	1.71	
U/V	24.0%	19.8%	18.3%	19.6%	15.7%		21.7%	18.8%	18.0%	19.8%	15.5%	
W/V	10.7%	7.7%	6.8%	6.7%	8.7%		11.0%	7.9%	6.9%	6.7%	7.7%	
Wannier spreads	5.78	5.35	4.66	4.42	4.12		5.73	5.05	4.77	4.21	3.83	
$5d$	$SrTaO_3$	$SrWO_3$	$SrReO_3$	$SrOsO_3$	$SrIrO_3$	$SrPtO_3$	$CaTaO_3$	$CaWO_3$	$CaReO_3$	$CaOsO_3$	$CaIrO_3$	$CaPtO_3$
U	3.48	3.17	3.12	3.29	3.36	2.34	2.94	2.86	2.96	3.17	3.24	2.47
J	0.45	0.47	0.48	0.50	0.52	0.50	0.45	0.47	0.48	0.50	0.52	0.51
V	13.71	14.44	14.94	15.63	16.13	16.69	13.81	14.52	15.08	15.67	16.26	16.78
J_{bare}	0.55	0.58	0.60	0.63	0.65	0.67	0.56	0.59	0.61	0.63	0.66	0.68
W	1.60	1.28	1.13	1.16	1.30	1.62	1.66	1.32	1.16	1.16	1.35	1.71
J_{screened}	0.41	0.40	0.39	0.39	0.40	0.44	0.42	0.41	0.40	0.40	0.40	0.44
U'	2.55	2.20	2.12	2.24	2.28	1.28	2.02	1.89	1.95	2.12	2.16	1.39
U/V	25.3%	21.9%	20.9%	21.0%	20.8%	14.0%	21.3%	19.6%	19.6%	20.2%	19.9%	14.7%
W/V	11.6%	8.8%	7.5%	7.4%	8.0%	9.7%	12.0%	9.0%	7.7%	7.4%	8.3%	10.1%
Wannier spreads	6.99	6.14	6.08	5.35	5.20	4.93	6.74	5.96	5.65	5.26	4.93	4.75

$4d^4$ $SrRuO_3$. The U decreases initially from $4d^1$ (3.55 eV) to $4d^3$ $SrTcO_3$ (3.03 eV), then increases to 3.40 eV at $4d^4$ $SrRuO_3$, and finally decreases to 2.86 eV at $4d^5$ $SrRhO_3$. The resulting U values for the $4d$ series, for instance $4d^1$ $SrNbO_3$, is consistent with the 3.2 eV reported in Ref. [122] and 3.0 eV reported in Ref. [66], and for $SrMoO_3$ (with t_{2g}-t_{2g} approximation), 2.8 [123] and 3.12 eV (with d-dp approximation) in Ref. [82]. The increase of U from $4d^3$ to $4d^4$ is only 0.37 eV smaller than the increase from $3d^3$ to $3d^4$ (0.69 eV). The stronger crystal field and delocalization of $4d$ induce a larger splitting between t_{2g} and e_g states compared with those in $3d$, resulting in a weaker screening effect from unoccupied states. Therefore, the d-d contribution in $4d$ is smaller than in $3d$, and excluding the d-d screening induces a less pronounced enhancement of U from $4d^3$ to $4d^4$.

Some notable observations include the following: (1) The fully screened interaction W in $4d$ is comparable to those of $3d$ ABO_3, but the (full) screening effect in $3d$ is significantly stronger than in $4d$. (2) Despite the generally smaller bare V in $4d$ than in $3d$ due to less localized d orbitals, the U in $4d$ is approximately 0.2 eV larger than in $3d$, indicating that the summations of d-p and rest screening in $4d$ are remarkably weaker than in $3d$ ABO_3. (3) The only difference in the trends of Hubbard U between the $3d$ and $4d$ series occurs from d^2 to d^3: in $3d$ ABO_3, $3d^2$ $SrCrO_3$ and $3d^3$ $SrMnO_3$ host roughly same partial screen strength (U/V), while in $4d$, the U/V in $4d^2$ $SrMoO_3$ is weaker than in $4d^3$ $SrTcO_3$, hinting that the enhanced d-d screening from $4d^2$ to $4d^3$ is not as pronounced as in the $3d$ series due to the larger crystal field splitting between the t_{2g} and e_g states.

In $5d$ ABO_3, the bare interaction V is even smaller compared to the $4d$ and $3d$ series due to the less localized nature of $5d$ orbitals. Additionally, both bare V and fully screened W exhibit similar behaviors as in $3d$ and $4d$ series. However, the trend of Hubbard U is slightly different. The maximum value of partial screen strength U/V is still located at $5d^4$ $SrOsO_3$, but the amplitude of the enhancement from $5d^3$ to $5d^4$ is smaller compared with the jumps in $3d$ and $4d$. The configurations from $5d^3$ to $5d^5$ host roughly the same strength of partial screenings, as shown in Fig. 4(f) and Table II. The

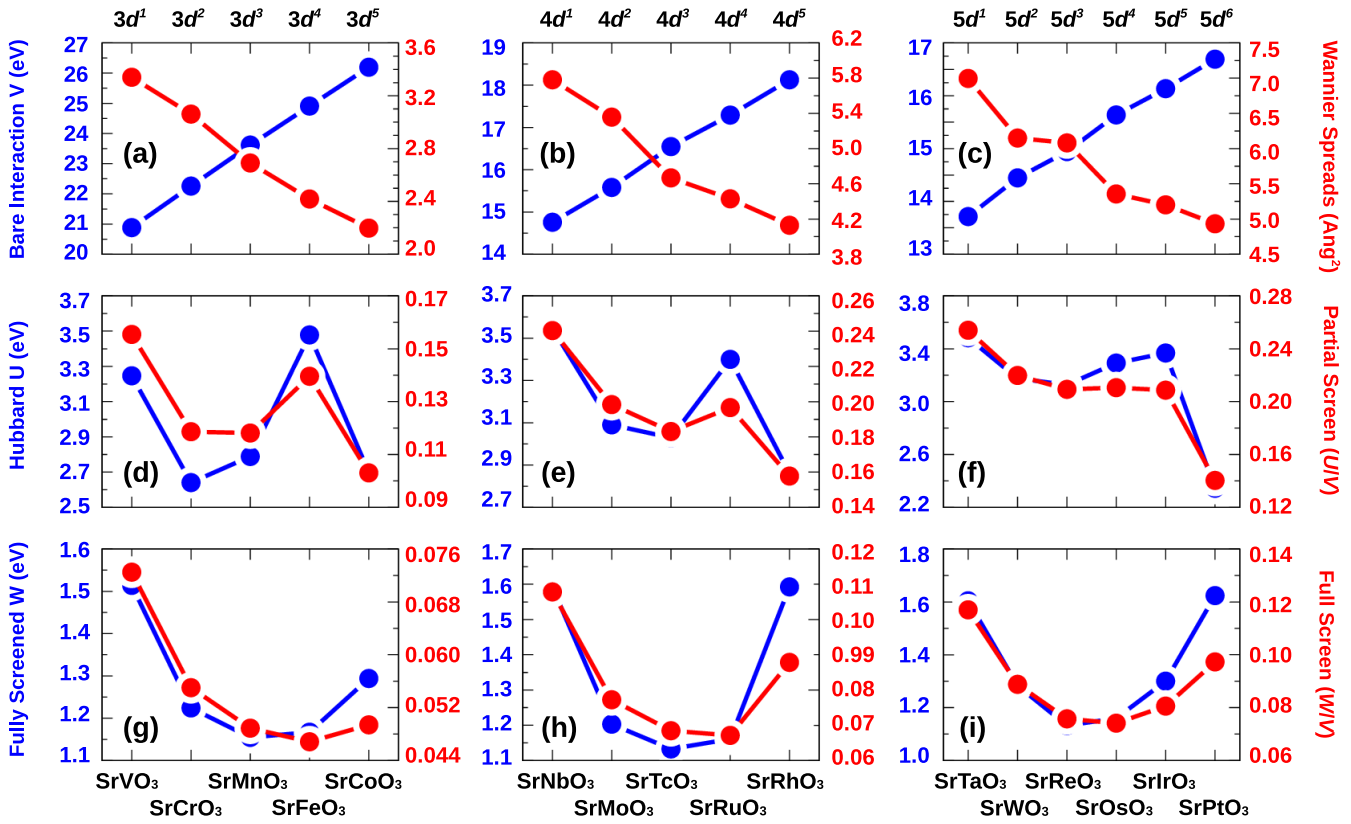

FIG. 4. The cRPA obtained interaction parameters for SrBO$_3$ (B = V to Fe, Nb to Ru, and Ta to Os) within d-dp approximation. Top panels: bare interaction V (blue) vs spreads (red) of d orbitals. Middle panels: Hubbard interaction U (blue) (partially screened interaction) vs partial screening (red) (U/V). Bottom panels: fully screened interaction W (blue) vs full screening (red) (W/V).

bare V increases from 14.94 eV ($5d^3$ SrReO$_3$) to 15.64 eV ($5d^4$ SrOsO$_3$) and 16.14 eV ($5d^5$ SrIrO$_3$). Hence, the U slightly increases from 3.13 to 3.37 eV from $5d^3$ to $5d^5$. At $5d^6$ SrPtO$_3$, U drops to 2.34 eV because the d-p screening contributes more than d-d screening, as the O-2p peak below E_f merges with the hybridization peak at E_f, forming a high peak and enhancing the d-p screening.

Hund's interaction. The bare (J_{bare}), partially screened (J), and fully screened (J_{screened}) Hund's exchanges are derived from the off-diagonal matrix elements of the interaction matrix (Table II). The evolution of Hund's interactions for the 3d, 4d, and 5d series follows the same tendencies, and we will use 3d as an example. In the 3d SrBO$_3$ series, partially screened Hund's exchange J monotonously increases from 0.63 ($3d^1$ SrVO$_3$) to 0.73 eV ($3d^5$ SrCoO$_3$), exceeding the J within the t_{2g}-t_{2g} approximation (Table III). These values align with the J values commonly used in previous DFT + U or DFT + DMFT calculations for ABO$_3$ and ABO$_2$ materials [124–127]. Similar to partially screened J, the bare exchange interaction J_{bare} also monotonously increases with atomic number from 0.74 eV ($3d^1$ SrVO$_3$) to 0.88 eV ($3d^5$ SrCoO$_3$). This indicates that both J and J_{bare} are determined by the degree of d-orbital localization, rather than following the tendencies of W and U. The more localized the d orbitals, the stronger J and J_{bare}. In contrast to J and J_{bare}, the fully screened J_{screened} follows the behavior of Coulomb interactions, i.e., the fully screened W, with a local minimum at $3d^3$ SrMnO$_3$. The J_{screened} values are 0.55 eV for $3d^1$ SrVO$_3$, 0.51 eV for $3d^2$ SrCrO$_3$, 0.50 eV for $3d^3$ SrMnO$_3$, 0.53 eV for $3d^4$ SrFeO$_3$, and 0.59 eV for $3d^5$.

The above discussion about J implies that only the full screening effect significantly modifies the J values, while both J and J_{bare} are primarily influenced by orbital localization. It is worth noting that, compared with U, W, and V (∼1.0 eV), the amplitudes of J_{bare}, J, and J_{screened} are an order of magnitude smaller (∼0.1 eV). Therefore, quantitative comparisons between the same period may not be as instructive as Coulomb interactions.

Finally, we delve into the outcomes of intraorbital Coulomb repulsion U', as presented in Table II. For 3d, 4d, and 5d series, U' consistently yields $U' = U - 2J$ due to the rotational symmetry, confirming the robustness of our cRPA calculations. The behavior of U' mirrors that of U.

D. t_{2g}-t_{2g} approximation for Sr-based 3d series

Within the t_{2g}-t_{2g} approximation, the t_{2g}-projected local orbitals within the energy window $\mathbb{W}_{t_{2g}}$ (Table I) result in "more extended" t_{2g} Wannier orbitals. The charge transfer energy and the hybridization between the t_{2g} and O-2p bands contribute to the finite weight/tail of the t_{2g} Wannier functions at the O sites. Consequently, a smaller d-p charge transfer energy (Δ_{dp}) leads to more extended projected t_{2g} orbitals. This tendency is evident in the 3d SrBO$_3$ bands and t_{2g} Wannier orbital

TABLE III. Bare V, Hubbard U, and fully screened W interactions, and corresponding Hund's exchange J_{bare}, J, and J_{screened} between t_{2g} orbitals within t_{2g}-t_{2g} approximation for SrMO$_3$ (M = V, Cr, Mn, Fe, Co, Nb, Mo, Tc, Ru, Rh, Ta, W, Re, Os, Ir, and Pt) perovskites. Their Wannier orbital spreads are also shown. All the energy units are in eV.

	d^1	d^2	d^3	d^4	d^1	d^2	d^3	d^4
3d	$SrVO_3$	$SrCrO_3$	$SrMnO_3$	$SrFeO_3$	$CaVO_3$	$CaCrO_3$	$CaMnO_3$	$CaFeO_3$
U	3.32	2.95	1.98	1.46	3.38	3.08	2.24	1.70
J	0.46	0.43	0.38	0.36	0.46	0.44	0.40	0.38
V	16.22	16.43	16.00	15.88	16.20	16.54	16.18	16.19
J_{bare}	0.56	0.54	0.50	0.48	0.56	0.54	0.51	0.49
W	0.99	0.71	0.57	0.54	1.01	0.72	0.59	0.56
J_{screened}	0.36	0.30	0.26	0.26	0.36	0.31	0.27	0.27
U'	2.34	2.00	1.10	0.63	2.41	2.13	1.33	0.82
U/V	20.4%	17.9%	12.3%	9.2%	20.8%	18.6%	13.8%	10.4%
W/V	6.1%	4.2%	3.5%	3.3%	6.2%	4.3%	3.6%	3.4%
Wannier spreads	5.85	6.80	8.70	9.15	6.00	6.733	8.50	9.09
4d	$SrNbO_3$	$SrMoO_3$	$SrTcO_3$	$SrRuO_3$	$CaNbO_3$	$CaMoO_3$	$CaTcO_3$	$CaRuO_3$
U	3.20	3.12	2.88	2.19	2.80	2.92	2.87	2.54
J	0.33	0.33	0.31	0.28	0.29	0.31	0.31	0.29
V	11.52	11.69	11.77	11.40	10.41	11.35	11.74	11.53
J_{bare}	0.42	0.41	0.39	0.35	0.36	0.39	0.39	0.36
W	0.99	0.64	0.51	0.45	0.88	0.64	0.52	0.46
J_{screened}	0.27	0.22	0.19	0.17	0.23	0.22	0.19	0.17
U'	2.52	2.43	2.20	1.54	2.23	2.26	2.19	1.87
U/V	27.7%	26.6%	24.4%	19.2%	26.9%	25.7%	24.4%	21.9%
W/V	8.5%	5.5%	4.3%	3.9%	8.4%	5.6%	4.4%	4.0%
Wannier spreads	7.43	8.11	8.83	10.31	11.01	9.21	9.00	10.40
5d	$SrTaO_3$	$SrWO_3$	$SrReO_3$	$SrOsO_3$	$CaTaO_3$	$CaWO_3$	$CaReO_3$	$CaOsO_3$
U	3.01	3.06	3.02	2.72	2.39	1.97	3.44	3.26
J	0.32	0.32	0.30	0.27	0.34	0.30	0.29	0.28
V	10.65	11.18	11.01	10.72	11.23	10.68	10.79	10.74
J_{bare}	0.40	0.40	0.38	0.35	0.42	0.38	0.37	0.35
W	0.98	0.71	0.54	0.47	0.95	0.65	0.55	0.48
J_{screened}	0.26	0.23	0.19	0.17	0.27	0.22	0.19	0.17
U'	2.39	2.38	2.36	2.09	1.74	1.39	2.78	2.60
U/V	28.2%	27.4%	27.4%	25.4%	21.3%	18.4%	31.8%	30.3%
W/V	9.1%	6.4%	4.9%	4.4%	8.4%	6.0%	5.0%	4.5%
Wannier spreads	8.58	7.76	8.94	10.59	6.92	9.52	9.74	10.60

spreads: as the Δ_{dp} decreases from $3d^1$ $SrVO_3$ to $3d^4$ $SrFeO_3$ (as illustrated in Fig. 1 by the splitting between d and O-2p states), the t_{2g} orbitals become more extended accordingly [as depicted in Fig. 5(a) with larger Wannier spreads].

The interaction parameters obtained from t_{2g}-t_{2g} approximation are detailed in Table III, and their evolution and the relationship between the most effective factor within the series are illustrated in Fig. 5. In Figs. 5(a)–5(c) and Table III, the unscreened bare interaction $V_{t_{2g}}$ within the t_{2g}-t_{2g} model does not increase with d-electron count as $V_{d\text{-}dp}$ does in the d-dp model. Additionally, the values of $V_{t_{2g}}$ are generally smaller than the values of $V_{d\text{-}dp}$ due to the greater delocalization of projected t_{2g} orbitals in the t_{2g}-t_{2g} model. For further comparison between ours and previous computations on the interaction parameters for the ABO_3 compounds based on the t_{2g}-t_{2g} approximation, we refer the readers to the references in Refs. [66,69,76,91,120,128–133].

We then explore the trends in the early series of 3d TMOs, specifically from $3d^1$ to $3d^3$. It is worth noting that the interaction parameters for the late series of $3d^4$, $3d^5$, $4d^4$, $4d^5$, and $5d^5$ obtained from t_{2g}-t_{2g} are not considered reliable due to significant hybridization between t_{2g} bands and O-2p bands. High-quality Wannier band projections depend on the choice of the energy window (Table I). For $3d^4/4d^4/5d^5$, an empirical energy window was used, resulting in t_{2g} Wannier projections that closely match the original DFT bands.

In the early 3d series ($3d^1$–$3d^4$), V fluctuates within a relatively small energy window, ranging from 15.88 eV ($3d^4$ $SrFeO_3$) to 16.44 eV ($3d^2$ $SrCrO_3$). Conversely, Wannier orbital spreads exhibit a monotonous increasing tendency from 5.86 Å^2 ($3d^1$) to 9.15 Å^2 ($3d^4$). The Wannier orbital spreads in the t_{2g}-t_{2g} approximation are generally larger than those in the d-dp approximation, suggesting that these correlated orbitals are more delocalized within the t_{2g}-t_{2g} approximation. Consequently, $V_{t_{2g}}$ is smaller than $V_{d\text{-}dp}$, as shown in Tables II and III.

The fully screened Coulomb interaction W significantly decreases from $3d^1$ $SrVO_3$ (0.99 eV) to $3d^4$ $SrFeO_3$ (0.54 eV).

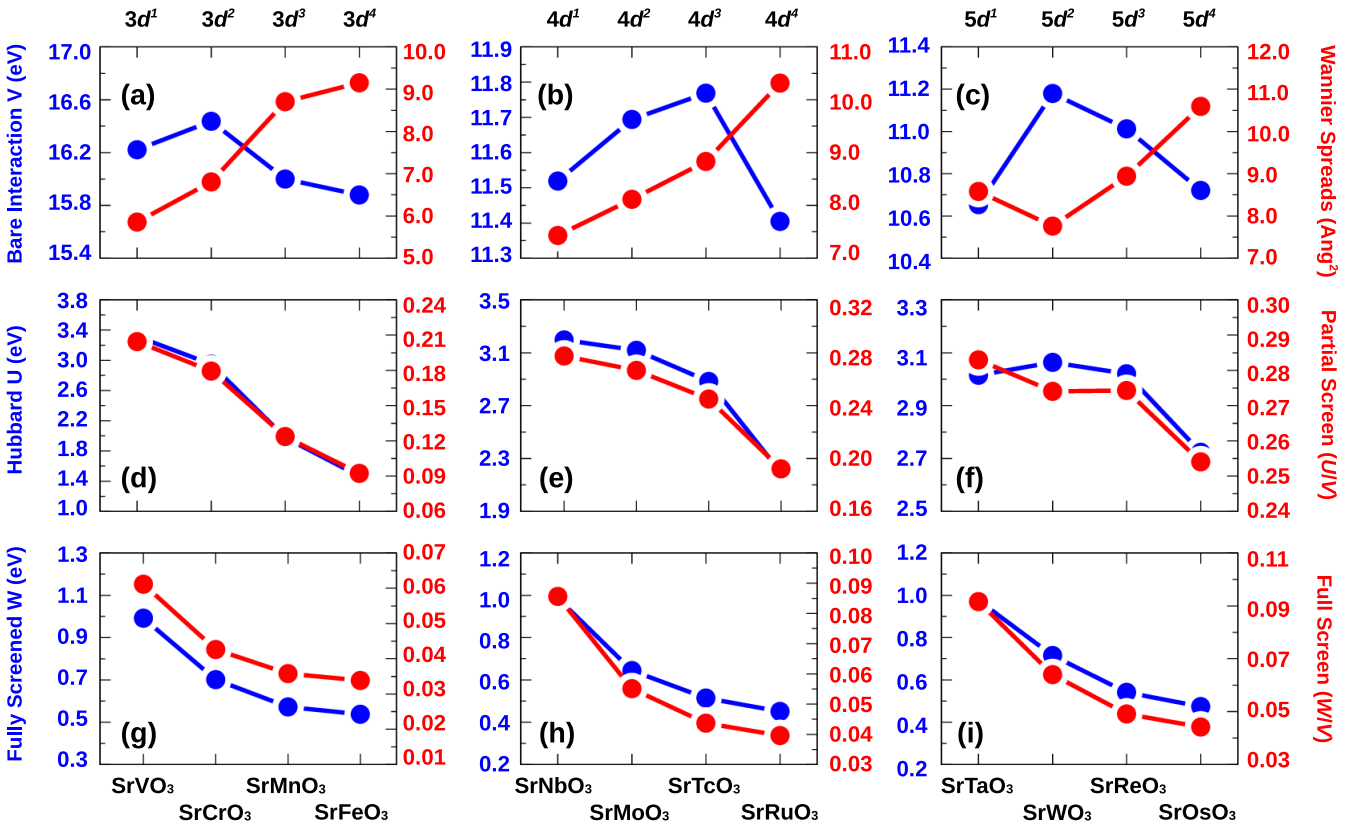

FIG. 5. Bare interaction V vs spreads of t_{2g} orbitals (upper panels), Hubbard interaction U (partially screened interaction) vs partial screening (U/V) (middle panels), and fully screened interaction W vs full screening (W/V) (bottom panels) of SrBO$_3$, within the t_{2g}-t_{2g} approximation.

The reduction of $W_{t_{2g}}$ is more pronounced than $W_{d\text{-}dp}$ within the d-dp approximation. The constancy of the bare interaction V from $3d^1$ to $3d^4$ indicates that the decrease in W is attributed to the increasing full screening effects with the increasing atomic number, consistent with the trends observed in the $3d$ series within the d-dp approximation. Due to the bandwidth reduction, the distance between unoccupied and occupied states is decreased, contributing to an enhanced total possibility of forming particle-hole excitations and leading to larger polarity and screening effects. Specifically, the p-t_{2g} and t_{2g}-e_g channels contribute increasingly to the screening from $3d^1$ SrVO$_3$ to $3d^4$ SrFeO$_3$ due to the p and e_g Kohn-Sham bands approaching the Fermi level [as shown in the DOSs in Figs. 1(a)–1(d)]. Quantitatively, the ratio W/V is about twice larger in $3d^1$ SrVO$_3$ (0.061) than in $3d^4$ SrMnO$_3$ (0.033), indicating that the strength of the full screening effect in SrMnO$_3$ is almost twice as strong as in SrVO$_3$ (Table III).

The partially screened Coulomb interaction U significantly decreases from $3d^1$ SrVO$_3$ to $3d^4$ SrFeO$_3$, with the reduction of $U_{t_{2g}}$ being more pronounced than $U_{d\text{-}dp}$ within the d-dp approximation. While the t_{2g}-t_{2g} is eliminated in this case, the screening contribution within d orbitals mainly stems from the t_{2g}-e_g channel, which is preserved in t_{2g}-t_{2g} while not in d-dp approximation. Consequently, U exhibits a similar behavior as W for the early $3d$ series within the t_{2g}-t_{2g} approximation.

In contrast to $J^{d\text{-}dp}$ and $J^{d\text{-}dp}_{\text{bare}}$ within the d-dp model, which all increase with the number of d electrons (the exception is $J^{d\text{-}dp}_{\text{screened}}$, which exhibits an almost constant value), the t_{2g}-t_{2g} Hund's exchange interactions $J_{t_{2g}}$, J_{bare}, and J_{screened} within the t_{2g}-t_{2g} approximation slightly decrease with the number of d electrons (Table III). The elimination of t_{2g}-t_{2g} transitions in the calculation of $J_{t_{2g}}$ suggests that screening effects induced by t_{2g}-e_g transitions are responsible for the decreasing behavior of $J_{t_{2g}}$. The decreasing behavior of J_{screened} indicates that t_{2g}-t_{2g} also contributes to the reduction of J_{screened}. Despite the apparent influence of t_{2g}-t_{2g} screening on J, the degree of orbitals localization also plays a role, as evidenced by the monotonous decrease observed in J_{bare} within the t_{2g}-t_{2g} Hamiltonian. This suggests that both the screening within d-orbital transitions and the localization of orbitals are decisive to J, with $J_{t_{2g}}$ being smaller within the t_{2g}-t_{2g} Hamiltonian than J_{d-dp} within the d-dp Hamiltonian.

E. t_{2g}-t_{2g} approximation for Sr-based 4d and 5d series

In the $4d$ and $5d$ SrBO$_3$ series, the evolution of DFT bands exhibits similarities with $3d$ SrBO$_3$ compounds (Figs. 2 and 3). However, there are notable differences, such as (1) larger crystal field splittings in $4d$ and $5d$ compounds, leading to increased d-p charge transfer energy $\Delta(dp)$ and reduced screening in d-p channels. (2) The Wannier spreads in the $4d$ and $5d$ series are generally larger than in $3d$, indicating more delocalized t_{2g} orbitals. As a result, the Coulomb interactions $W_{t_{2g}}$, $V_{t_{2g}}$, and $U_{t_{2g}}$ are expected to be smaller in $4d$ and $5d$

than those in the 3d series, varying within a small energy region and exhibiting a "constant" behavior. This prediction is supported by the obtained quantities (Table III), where $U_{t_{2g}}$ in the 4d and 5d series shows a general reduction, and it becomes almost constant in 5d. This conclusion is supported by Table III (taking U as an example): for the 3d series the U decreases from 3.32 eV ($3d^1$ $SrVO_3$) to 1.47 eV ($3d^4$ $SrFeO_3$), for the 4d series the U slightly decreases from 3.20 eV ($4d^1$ $SrNbO_3$) to 2.19 eV ($4d^4$ $SrRuO_3$), and for the 5d series the U merely decreases from 3.01 eV ($5d^1$ $SrTaO_3$) to 2.72 eV ($5d^4$ $SrOsO_3$).

The W is influenced by a delicate interplay between the full screening effect and the degree of localization of the Wannier t_{2g} orbitals. In addition to the contributions from the d-p and t_{2g}-e_g channel screenings discussed above, the t_{2g}-t_{2g} channel screening, which is also influenced by the crystal field splitting, also plays a role. This effect is expected to have a more pronounced impact on W as compared to U. Consequently, W exhibits similar trends across the 3d, 4d, and 5d series: for the 3d series, W decreases from 0.99 eV ($3d^1$ $SrVO_3$) to 0.54 eV ($3d^4$ $SrFeO_3$); for the 4d series, W decreases from 0.99 eV ($4d^1$ $SrNbO_3$) to 0.45 eV ($4d^4$ $SrRuO_3$); and for the 5d series, W decreases from 0.98 eV ($5d^1$ $SrTaO_3$) to 0.47 eV ($5d^4$ $SrOsO_3$).

The t_{2g} orbitals must be more delocalized in 4d and 5d oxides than in 3d oxides since the bare interaction V-3d is almost twice as large as that of 4d oxides (Table III). This observation aligns with the atomiclike basis, where the extension of the 4d atomic wave functions is larger than that of 3d oxides. In the 4d series, V monotonously increases with the rise in d-electron numbers, with a reduction of V at $4d^4$. This is attributed to the hybridization between Ru-t_{2g} and O-2p, giving rise to additional screening effects from O-2p. Along the lines of the 4d series, the 5d series should also exhibit similar tendency, with V increasing as the d-electron numbers increase until d-p band overlapping occurs. However, as shown in Fig. 5(c), the V of $5d^1$ $SrTaO_3$ is 10.65 eV, smaller than that of $5d^2$ $SrWO_3$ (11.18 eV) and $5d^3$ $SrReO_3$ (11.01 eV). The abnormal behavior in the 5d series is attributed to band hybridization between Sr-d and B-5d, as illustrated in Figs. 3(a) and 3(b), where d bands overlap Sr-d bands. This hybridization influences the degree of orbital localization, thus modifying V. Consequently, this hybridization also affects the Wannier spreads and renormalizes the value of V.

As indicated by the full screening strength W/V, within same period, e.g., for 3d, the W/V becomes smaller as d-electron numbers, indicating larger full screening strength. As we discussed above, this is due to the facts that (1) the increased band filling and bandwidth reduction makes the energy distance shorter, (2) more d states become occupied, leading to stronger d-d screening, and (3) smaller d-p charge transfer energy leads to larger d-p screening. Within the same main group, the full screening effects get weaker as indicated by the increasing W/V, e.g., the W/V is 0.061 for $3d^1$ $SrVO_3$, 0.085 for $4d^1$ $SrNbO_3$, and 0.091 for $5d^1$ $SrTaO_3$, which is due to the larger crystal field splitting.

The U/V provides information about the strength of partial screening, primarily from d-p screening and other screening contributions (mostly from Sr-d states). One would expect U/V to decrease (indicating increasing partial screening strength) with increasing d electrons within the same group. However, as shown in Table III, the decrease in U/V for the 4d and 5d series is not as pronounced as in the 3d series. For instance, in the 3d series, U/V decreases from 0.204 ($3d^1$ $SrVO_3$) to 0.092 ($3d^4$ $SrFeO_3$), while in the 5d series, it merely decreases from 0.282 ($5d^1$ $SrTaO_3$) to 0.254 ($5d^4$ SrOsO3), remaining almost constant. This phenomenon can be attributed to the slower decrease in p-d charge transfer energy and t_{2g}-e_g splitting in the 4d and 5d series. Within the same main group, the partial screening effects decrease, as indicated by the increasing U/V. For example, U/V values are 0.204 for $3d^1$ $SrVO_3$, 0.277 for $4d^1$ $SrNbO_3$, and 0.282 for $5d^1$ $SrTaO_3$. Consequently, on the first hand, $U^{t_{2g}}$ changes significantly in the 3d and 4d series, whereas it remains relatively constant in the 5d series with varying numbers of d electrons (Fig. 5). This effect can be attributed to screening, which has a stronger impact on the atomiclike Wannier basis of the 3d series compared to the delocalized nature of the 5d series. On the other hand, the behavior of $W^{t_{2g}}$ is consistent across all 3d, 4d, and 5d series.

Unlike V, U, and W, the behavior of J, J_{bare}, and J_{screened} is almost consistent across the 4d and 5d series, with these parameters monotonically decreasing as the number of d electrons increases. However, there is one exception observed in $5d^1$ $SrTaO_3$, where both J and J_{bare} are almost the same as those of $5d^2$ $SrWO_3$. This deviation can be attributed to the hybridization between Ta-5d and Sr-4d, as discussed above. All Hund's exchange J parameters exhibit only minor variations within a narrow energy range.

F. d-dp or t_{2g}-t_{2g} approximations and their scope of applications

We conducted cRPA calculations using both t_{2g}-t_{2g} and d-dp approximations to determine Coulomb and Hund's interaction parameters. It is important to note that the obtained parameters are model dependent. While direct comparison between the quantities from these two approximations is not feasible, for some cases (as discussed later, with strong d-p hybridization), notable differences arise, especially in late TM ABO_3 materials. For instance, in $3d^3$ $SrMnO_3$, the t_{2g}-t_{2g} approximation yields a Hubbard $U_{t_{2g}}$ of 1.98 eV, whereas the d-dp approximation gives $U_{d\text{-}dp} = 2.79$ eV. This discrepancy arises from the spread of Mn-d characters onto O ligands due to d-p hybridization.

In all 3d, 4d, and 5d series, as d-electron filling increases, O-2p bands approach B-d bands, leading to overlapping and reduced d-p charge transfer energy $\Delta(dp)$. The increased d-p hybridization transfers more d characters to the ligand O sites. Despite the bandwidth reduction, the t_{2g} Wannier orbitals become more delocalized. However, this strong d-p hybridization and band overlapping render t_{2g}-t_{2g} less appropriate for late TM perovskites. In early TM perovskites, both models yield a valid effective low-energy description, ensuring similar results in many-body calculations. The reliability of the t_{2g}-t_{2g} approximation diminishes around the d^4 or d^5 configuration, as seen in $3d^4$ $SrFeO_3$, $4d^4$ $SrRuO_4$, and $5d^5$ $SrIrO_3$, where non-negligible t_{2g} characters are present even before t_{2g} bands touch O-2p bands [see Figs. 1(d), 2(d), and 3(e)], there is already nonignorable t_{2g} characters

ranging from ∼−6.0 to ∼−2.0 eV. Additionally, the magnetic configuration plays a role; in materials such as $3d^3$ $SrMnO_3$ and $3d^4$ $SrFeO_3$, high-spin magnetic states result in occupied e_g orbitals, favoring a d-dp model for interaction parameter calculations.

The core problem in cRPA calculations within the t_{2g}-t_{2g} approximation for ABO_3 perovskites is the d-p bands' overlapping and hybridization. Strong d-p hybridization makes it challenging to project onto t_{2g} bands, hindering the obtainment of unique and trustworthy interaction parameters. This issue is effectively addressed with d-dp approximations, as they handle d-p hybridization in the model constructions.

In the t_{2g}-t_{2g} model, Wannier functions are constructed from the threefold-degenerate low-energy t_{2g} bands only. While this procedure projects most t_{2g} character onto the Wannier bands, significant O-2p admixing occurs due to heavy p-d hybridization. Stronger d-p hybridization results in more "extended" t_{2g} Wannier orbitals, showing pronounced tails on the O ligand sites. In early TM ABO_3 systems, such as $3d^1$ $SrVO_3$ or $4d^1$ $SrNbO_3$, the t_{2g} tails are not strongly pronounced due to the large energy gap between the TM-d and O-2p states. The t_{2g} character in the energy region from −8.0 to −4.0 eV, as indicated by the DOS, suggests that the t_{2g}-t_{2g} approximation effectively captures the realistic orbital physics of t_{2g} orbitals, making it a suitable approximation for early transition-metal ABO_3 systems. As the system approaches d^4 configurations, exemplified by $3d^3$ $SrMnO_3$, the t_{2g} bands may be gapped with O-2p bands. However, relying on projected t_{2g} Wannier bands and obtaining interaction parameters for subspace many-body calculations might be questionable when neglecting intersite interaction terms. If the orbitals are overly extended, significant intersite interactions may arise, questioning the Hubbard-type model (e.g., in DMFT) with only on-site terms. The divergence between $U_{t_{2g}}$ and $U_{d\text{-}dp}$ underscores the importance of including p bands for late transition-metal ABO_3 perovskites to address the d-p hybridization issue.

Within the d-dp approximation, more precise Wannier projections (for d orbitals) are achieved by constructing projected orbitals from the entire d-p group of bands including all d characters. Therefore, applying the d-dp approximation for TM ABO_3 perovskites later than d^3 is preferable.

However, a new question emerges regarding the increasing d-p hybridization: as it becomes more pronounced, off-diagonal matrix elements related to O-2p orbitals in the interaction parameters matrix, such as U_{dp} or U_{pp}, cannot be neglected. Previous research suggests that neglecting U_{pp} might be a reasonable approximation since O-2p states are typically delocalized and fully occupied (except for charge transfer insulator such as cuprate superconductor). Yet, in studies involving e_g-orbital materials such as $LaNiO_3$ [134], U_{dp} terms may be crucial as e_g-p interactions/hybridization become stronger than t_{2g}-p hybridization.

G. Limitations of the cRPA method

Before concluding, we would like to briefly dicuss the potential limitations of the cRPA method: (i) dynamical screening effect and frequency dependence of interaction parameters, (ii) the issue of double counting in polarizability, and (iii) the treatment of magnetism.

Dynamical screening and frequency dependence of $U(\omega)$. The Coulomb interaction U derived from cRPA is frequency dependent, reflecting the dynamical nature of screening effects from other atoms/orbitals in materials. However, practical implementations or computational approaches, such as DFT + U or DFT + DMFT, typically employ the static limit ($\omega \to 0$) for computational feasibility. This static approximation leads to the overscreening, as highlighted in Refs. [91,92,135–139]. While more sophisticated methods, such as constrained functional renormalization group (cfRG) [140], mitigate overscreening by including non-RPA contributions, their high computational cost limits their applicability to simple model systems.

Using a dynamical quantum impurity solver to account for the full frequency dependence in DFT + DMFT calculations can introduce additional challenges. Specifically, the inclusion of $U(\omega)$ often results in an unrealistic narrowing of the bandwidth, which deviates from experimental observations. This discrepancy arises from the implicit double counting of correlation effects already present in the DFT exchange-correlation functional. To address this, hybrid methods such as screened exchange combined with dynamical DMFT have shown promise due to error cancellation between dynamical screening and nonlocal exchange effects [141].

We note that the calculations presented in this work focus on the overall trend across a series of perovskite TMOs rather than the precise values of U. Therefore, the employed (static) cRPA ensures that our findings remain meaningful despite the static approximation limitations. Extending this work to include the dynamical screening effects within other more sophisticated methods such as hybrid frameworks or cfRG would be a valuable avenue for future research.

Double counting of polarizability χ. The RPA is a method that involves an infinite summation of bubble diagrams while neglecting others, such as exchange or ladder diagrams. Despite its simplicity, the RPA effectively captures long-range charge fluctuations, plasmon, high-energy scattering, and many-body dispersion effects, which are prominent in high-density metallic and semiconducting systems [98,99,142,143]. Consequently, RPA is well suited for constructing effective low-energy models.

The cRPA builds on this by excluding contributions from correlated orbitals when computing polarizability within the RPA framework. This is achieved by separating the total polarizability (χ_{tot}) into correlated polarizability (χ_c) and rest polarizability χ_r components. The effective interaction U is then calculated using only χ_r. The goal of this is to avoid double-counting effects when integrating DFT with more advanced many-body Hamiltonian approaches, as these methods explicitly account for correlations within the targeted orbitals. The assumption underpinning cRPA is that RPA-like bubble diagrams dominate the screening of local Coulomb interactions, making the formulation of cRPA exact under this assumption. Specifically, the fully screened interaction $W = V + V\chi^{\text{tot}}W$ can be expressed as $W = U + U\chi^c W$ with $\chi^c = \chi^{\text{tot}} - \chi^r$ and $U = V + V\chi^r U$, where V and U are bare and partially screened interactions, respectively, and χ^{tot}, χ^c, and χ^r are the total, correlated, and rest polarizabilities,

respectively. χ^c has already been included in the many-body Hamiltonian approaches, and therefore, one has to eliminate χ^r from χ^{tot}.

It is important to emphasize that the double-counting correction in cRPA is fundamentally different from the double-counting issue that arises when combining DFT and many-body methods like DMFT. The latter issue stems from the mismatch in the theoretical frameworks of DFT (density functional) and DMFT (Green's function), making it challenging to precisely identify and correct for the doubly counted contributions.

Impact of magnetism. The derived parameters are spin dependent when spin polarization is considered, as the screening varies for electrons with the same spin and those with opposite spins. Notably, the RPA method violates the Pauli exclusion principle in Hubbard-like models because its diagrammatic expansion includes self-interaction contributions for electrons with the same spin. This violation can be rectified using the spin-dependent cRPA formalism, which appropriately accounts for spin-specific interactions [136].

The static cRPA framework used in this work does not explicitly account for spin-dependent screening effects. In principle, spin-dependent cRPA can provide a more accurate description by distinguishing between same-spin ($\uparrow\uparrow, \downarrow\downarrow$) and mixed-spin ($\uparrow\downarrow, \downarrow\uparrow$) channels. However, the increased computational complexity has restricted its application to model systems [136].

In practical calculations, spin-independent U values derived from nonmagnetic DFT bands and nonmagnetic cRPA are often used as inputs for spin-polarized DFT + U or DFT + DMFT calculations. While this approach does not capture the full complexity of spin-dependent screening, it has been widely adopted and validated for describing magnetic properties in correlated materials. Incorporating spin-dependent screening effects in real materials remains an open challenge that merits further investigations.

In summary, while the current static and spin-independent cRPA approach has limitations, it remains a useful tool for studying trends in Coulomb interactions across material families. The frequency dependence of U, potential overscreening, and the absence of spin-dependent screening effects highlight areas where future investigations are needed. Addressing these challenges in future studies could further refine our understanding of correlated materials and their complex electronic interactions.

IV. CONCLUSION

Determining Coulomb and Hund's interactions from first principles for a given low-energy Hamiltonian is a necessary avenue for achieving a truly *ab initio* description of correlated materials within many-body calculations. Towards this goal, the cRPA method is an elegant approach that enables one to obtain the interaction parameters for orbitals within the low-energy correlated subspace. The central idea of the cRPA method is to exclude the contributions within the correlated orbitals when calculating the polarizability within the RPA. The aim of this constraint is essentially to avoid the double-counting problem when augmenting the DFT with more sophisticated many-body Hamiltonian approaches, since these methods focus only on the correlated orbitals and already account for the screening within these orbitals. In this regard, it is not meaningful to simply talk about interaction parameters without mentioning the low-energy Hamiltonian.

However, for perovskite TMOs with complicated multiband structures, the low-energy Hamiltonian spanning only TM-t_{2g} or entire TM-d states may not be well defined due to the strong hybridization with O-2p states. In this situation, the extended O-2p states have to be included in the low-energy Hamiltonian. Therefore, in the present work, we conducted systematic cRPA calculations of interaction parameters for the TM-d shell of ABO_3 perovskites (A = Sr, Ca; B = V to Co, Nb to Rh, and Ta to Pt) using two distinct approximations of the low-energy Hamiltonian. The first one is the widely used t_{2g}-t_{2g} model, and the other one is the d-dp model. For the t_{2g}-t_{2g} model, the low-energy Hamiltonian is determined by the TM-t_{2g} orbitals, and the interaction parameters are calculated for the same set of orbitals. For the d-dp model, the low-energy Hamiltonian is described by both TM-d and O-2p orbitals, while the interaction parameters are obtained only for the TM-d shell. For both models, SrBO_3 and CaBO_3 (see Appendix) yield similar trends for the interaction parameters over the occupancy of d orbitals.

Within the t_{2g}-t_{2g} framework, the bare Coulomb interaction V fluctuates within a small energy window (less than 1.0 eV), which is influenced by an interplay between bandwidth reduction and orbital delocalization with increasing d-electron number. This demonstrates the atomiclike behavior of ABO_3, especially for the 3d and 4d series, with V monotonously increasing as the d-electron number rises. This is because the 3-4d orbitals are more localized than the 5d orbitals and their orbital localization is not affected by Sr-4d hybridization. The partially screened Coulomb interaction U decreases with increasing d-electron number due to the enhanced t_{2g}-e_g and d-p screening, contributing significantly to the rest polarizability. The fully screened Coulomb interaction W also decreases monotonously due to the increasing full screening effects. Hund's interactions (J_{bare}, J, and J_{screened}) all decrease with rising d-electron numbers, implying that Hund's interactions are mediated by enhanced d-orbital delocalization.

However, for the d-dp model, we observed that U tends to exhibit a maximum at d^4 (for the 3d and 4d series) or d^5 (for the 5d series). This maximum arises from the competition between orbital localization and the d-d (and also d-p) screening effect. The V monotonously increases along the same period, indicating that it is predominantly influenced by orbital localization. The W is influenced by the interplay between the enhancement and reduction of full screening effects, resulting in a minimum at d^3 for 3d, 4d, and 5d perovskites. Both J and J_{bare} show similar tendencies as V, suggesting that they are determined by orbital localization, while J_{screened} exhibits a "decrease-increase" behavior (with a minimum at d^3, similar to W), indicating the dominant role of full screening effects in determining J_{screened}.

This work demonstrates that the actual value of U depends on the subtle competition between orbital localization and the strength of screenings excluding the contribution from correlated orbitals, which are in turn subject to the specific band structure modulated by the d-orbital filling. Moreover, this work highlights the importance of defining an

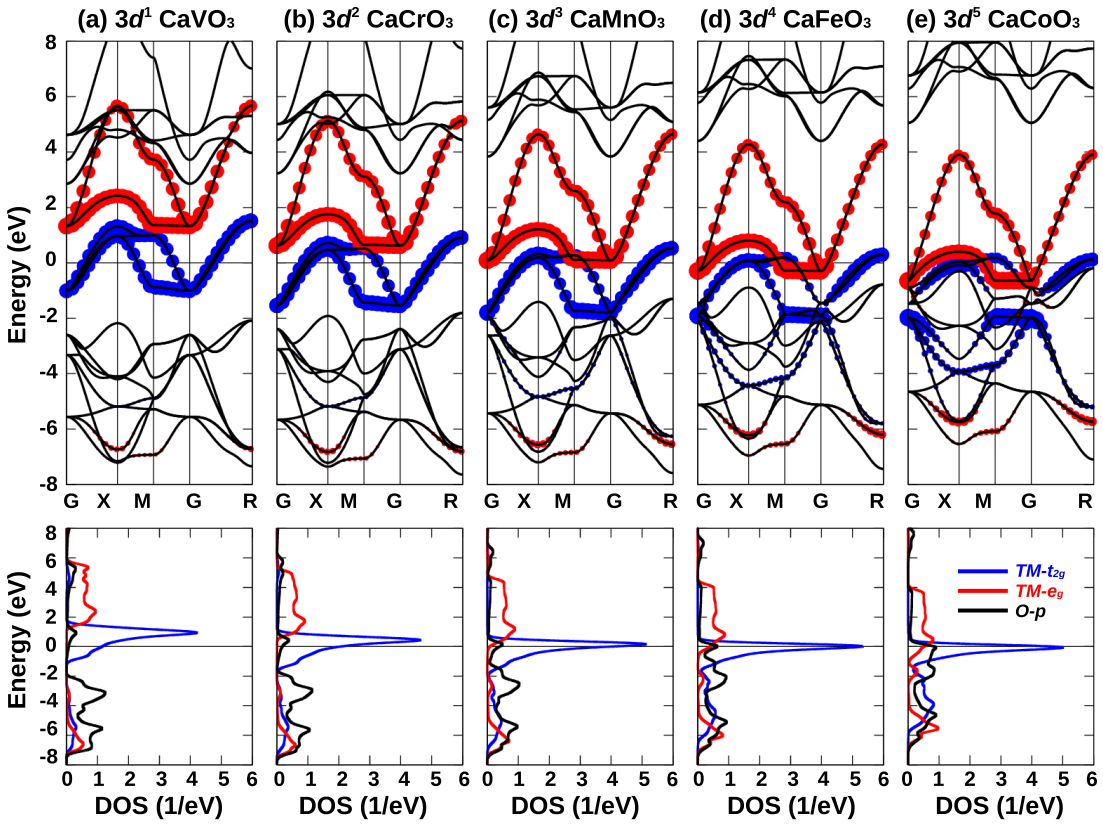

FIG. 6. DFT bands (top panels) and density of states (bottom panels) of CaBO$_3$ (B = V, Cr, Mn, Fe, and Co). The size of the blue and red points indicates contributions from t_{2g} and e_g orbitals.

appropriate low-energy Hamiltonian, which is directly linked to the physical meaning of the obtained U. The conclusion of this systematic study is general and can be extended to other materials and other physical scenarios.

ACKNOWLEDGMENTS

L.S. acknowledges the funding from the National Natural Science Foundation of China (Grant No. 12422407). L.S. and C.F. were supported by the Austrian Science Fund (FWF) SFB project ViCoM (Grant No. F41). C.F. acknowledges the funding by the European Union–Next Generation EU–"PNRR–M4C2, investimento 1.1-Fondo PRIN 2022"–"Superlattices of relativistic oxides" (ID No. 2022L28H97, CUP D53D23002260006). P.L. acknowledges the funding from the National Natural Science Foundation of China (Grants No. 52422112 and No. 52188101) and the Liaoning Province Science and Technology Planning Project (2023021207-JH26/103 and RC230958). Calculations have been done on the Vienna Scientific Clusters (VSC).

DATA AVAILABILITY

For the input and output files of the calculation examples discussed in this paper, please refer to [144].

APPENDIX

Interaction parameters for Ca-based 3d, 4d, and 5d series

To corroborate our findings in the discussion of SrBO$_3$ perovskites, we performed electronic structure and interaction parameter calculations for CaBO$_3$ perovskites. The trends observed in CaBO$_3$ are basically consistent with those in SrBO$_3$, reinforcing our earlier conclusions.

The band structures of CaBO$_3$ are shown in Figs. 6–8. The results of the interaction parameters obtained from the d-dp approximation are presented in Fig. 9 and the right panel of Table III. In Figs. 9(a)–9(c), the V for 3-5d CaBO$_3$ increases as the d orbitals become more localized, indicated by decreasing Wannier orbital spreads. V is larger in 3d than in 4d and 5d due to the more localized d orbitals in the 3d series. Hubbard U also exhibits a tendency similar to SrBO$_3$: local maxima occur at d^1 and d^4 for the 3d and 4d series, and d^1 and d^5 for the 5d series. Notably, the Hubbard U of 3d^4 CaFeO$_3$ (4.89 eV) is ∼1.4 eV stronger than in 3d^4 SrFeO$_3$, suggesting a greater contribution of d-d screening in 3d^4 CaFeO$_3$ to full screening. However, no significant differences are observed in their electronic bands and DOSs [compare Fig. 1(d) to Fig. 6(d)].

Within the t_{2g}-t_{2g} approximation (Fig. 10), basically all of Hund's exchange interaction parameters of CaBO$_3$ exhibit similar tendencies as in SrBO$_3$. All the bare V merely varies within a small energy window of about ∼1.0 eV. In the more extended 4d series the V follows atomiclike behavior: increases as d-electron filling for early transition-metal perovskites ($d \leqslant 3$). For the 5d series, the 5d^1 configuration is affected by the Ta-5d and Sr-4d hybridization, so both the Wannier localization and the V are modified by this hybridization, leading to the breaking down of the atomiclike behavior. The tendency of the fully screened W is the same

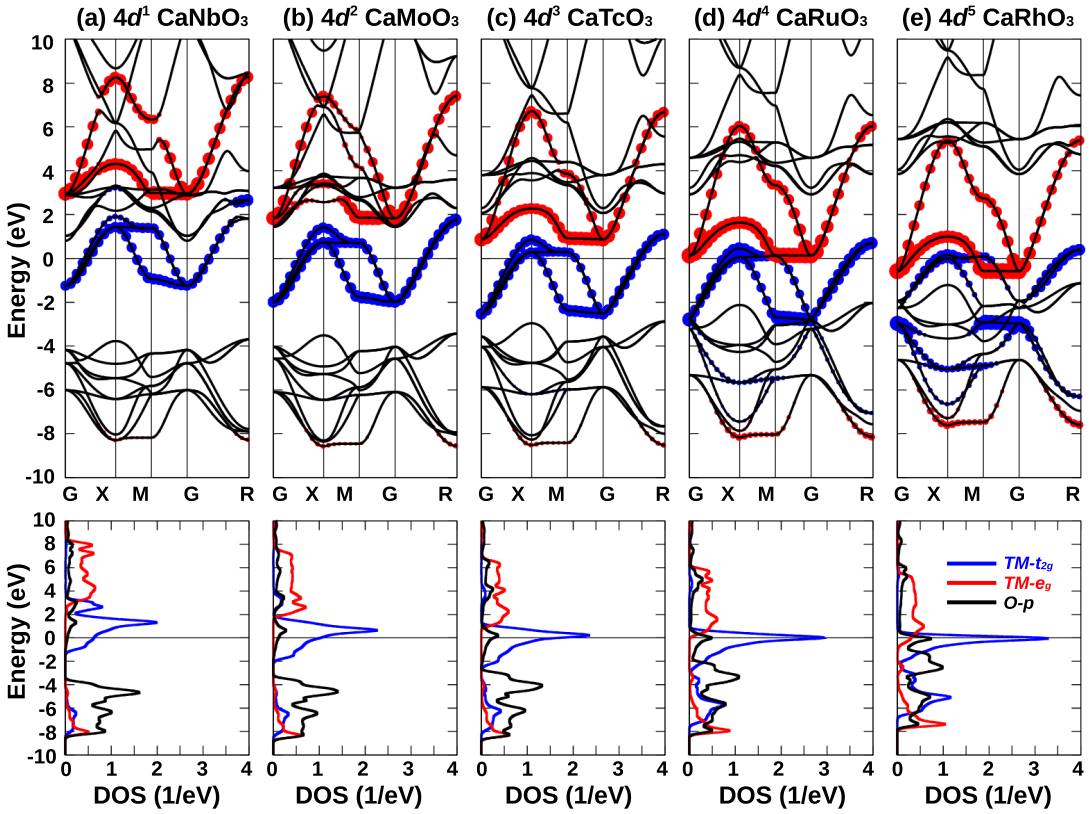

FIG. 7. DFT bands (top panels) and density of states (bottom panels) of CaBO$_3$ (B = Nb, Mo, Tc, Ru, and Rh). The size of the blue and red points indicates contributions from t_{2g} and e_g orbitals.

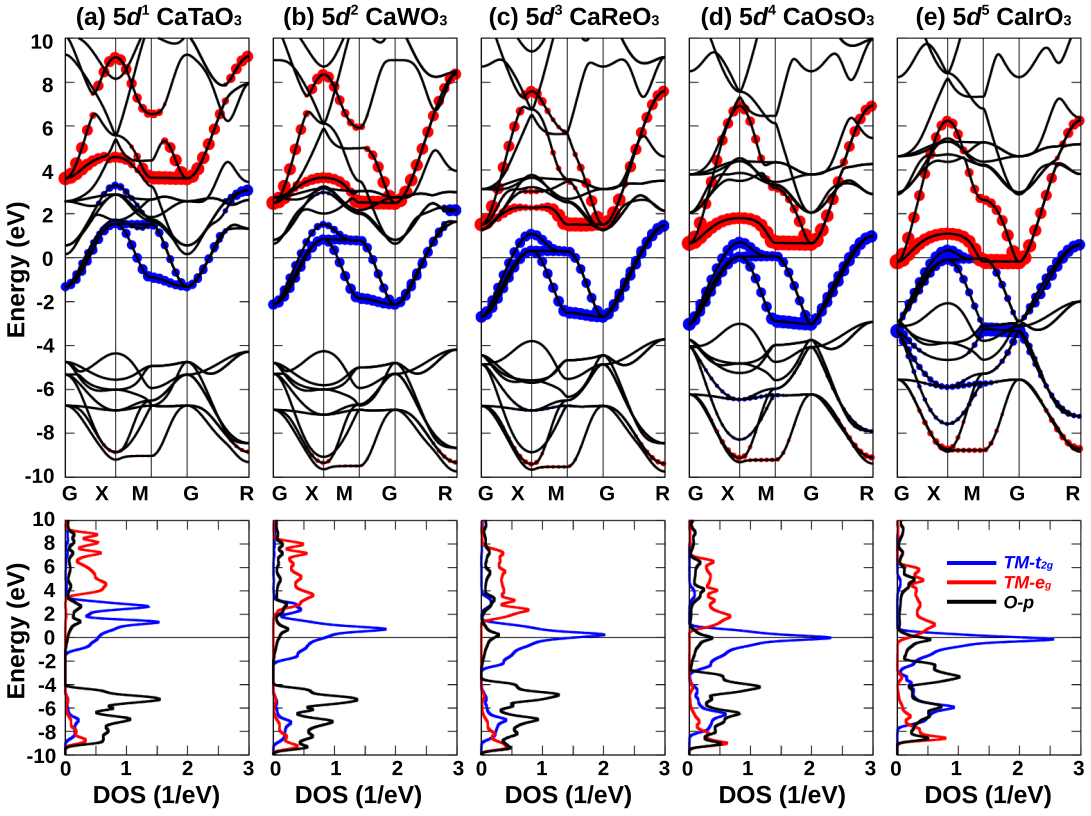

FIG. 8. DFT bands (top panels) and density of states (bottom panels) of CaBO$_3$ (B = Ta, W, Re, Os, and Ir). The size of the blue and red points indicates contributions from t_{2g} and e_g orbitals.

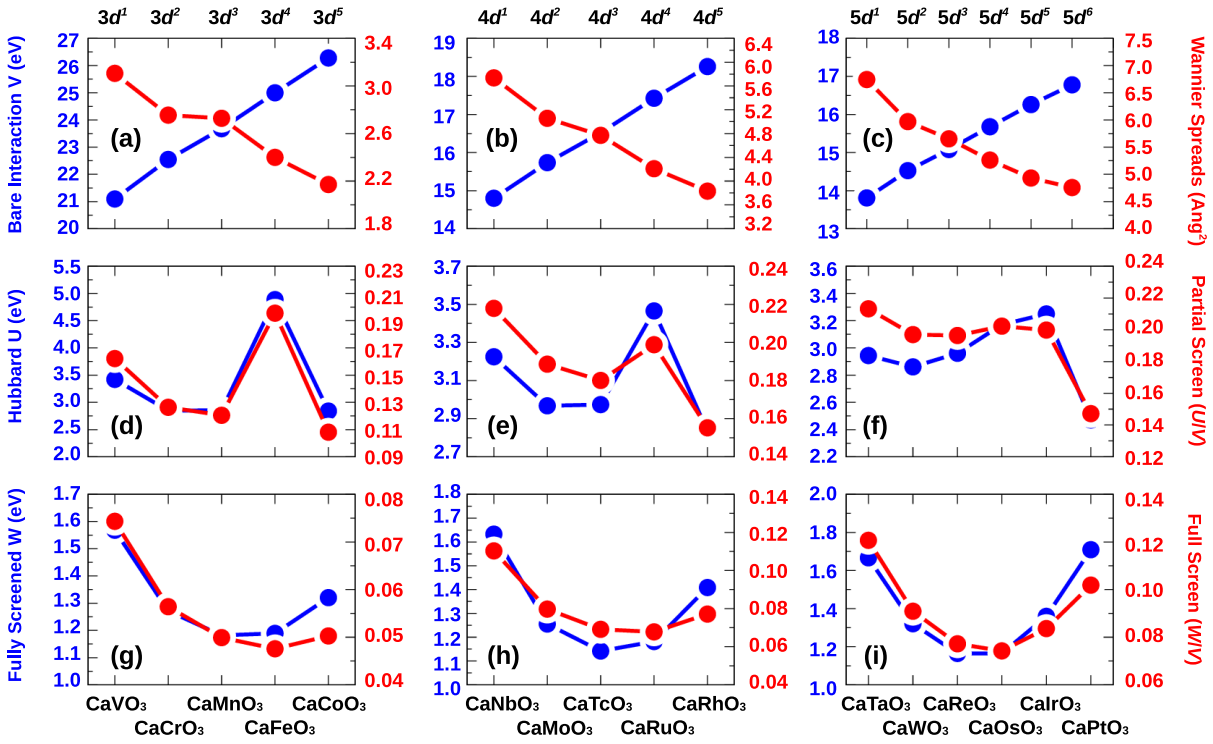

FIG. 9. Bare interaction V vs spreads of d orbitals (upper panels), Hubbard interaction U (partially screened interaction) vs partial screening (U/V) (middle panels), and fully screened interaction W vs full screening (W/V) (bottom panels) of CaBO$_3$, within the d-dp approximation.

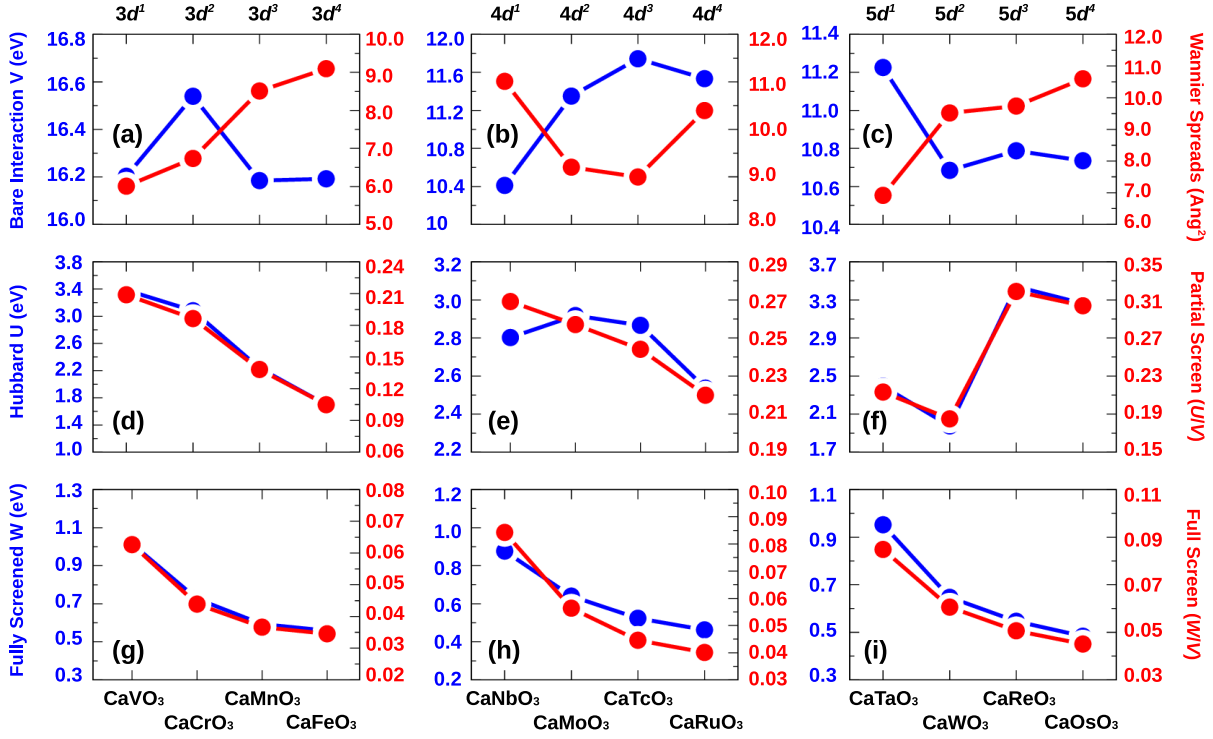

FIG. 10. Bare interaction V vs spreads of d orbitals (upper panels), Hubbard interaction U (partially screened interaction) vs partial screening (U/V) (middle panels), and fully screened interaction W vs full screening (W/V) (bottom panels) of CaBO$_3$, within the t_{2g}-t_{2g} approximation.

as in the Sr-based series: deceases as the d electron increases, indicating the full screening effect gets stronger. For both the $3d$ and the $4d$ series of $CaBO_3$, the tendency of Hubbard U is the same as in the $3d$ and $4d$ series of $SrBO_3$, i.e., they decrease as the d-electron filling increases. However, a different tendency is found for the $5d$ series. The Hubbard U's of $5d^1$ $CaTaO_3$ (2.39 eV) and $5d^2$ $CaWO_3$ (1.98 eV), are remarkably smaller than those in $5d^3$ $CaReO_3$ (3.44 eV) and $5d^4$ $CaOsO_3$ (3.26 eV). We attribute this to the Sr-$4d$ and TM-$5d$ hybridization as shown in the bands of $5d^1$ $CaTaO_3$ and $5d^2$ $CaWO_3$. The t_{2g} bands of $CaTaO_3$ and $CaWO_3$ are heavily overlapped. This enhances the Wannier spreads of projected t_{2g} orbitals and reduced the Hubbard U, and most importantly, the d-d screening is reduced. Thus the remaining d-p screening plays an effecttive role in reducing V to U at both $5d^1$ and $5d^2$ configurations.

Within the t_{2g}-t_{2g} approximation (Fig. 10), Hund's exchange J for $CaBO_3$ shows similar trends to $SrBO_3$. Bare V varies within a small energy window of $\sim$1.0 eV. In the more delocalized $4d$ series, V increases with d-electron filling for $d \leqslant 3$. For the $5d$ series, the $5d^1$ configuration is influenced by Ta-$5d$ and Sr-$4d$ hybridization, altering both Wannier localization and hence V. This breakdown of atomiclike behavior is evident. The fully screened W follows the same trend as in the Sr-based series: decreasing as the d electron filling increases, indicating a strengthening full screening effect. In both the $3d$ and the $4d$ series of $CaBO_3$, Hubbard U decreases with increasing d-electron filling, mirroring the trend in the $3d$ and $4d$ series of $SrBO_3$. However, a different trend is observed for the $5d$ series. The Hubbard U of $5d^1$ $CaTaO_3$ (2.39 eV) and $5d^2$ CaWO3 (1.98 eV) is significantly smaller than in $5d^3$ $CaReO_3$ (3.44 eV) and $5d^4$ $CaOsO_3$ (3.26 eV). This can be attributed to Sr-$4d$ and B-$5d$ hybridization, evident in the bands of $5d^1$ $CaTaO_3$ and $5d^2$ $CaWO_3$ (Fig. 8). The t_{2g} bands of $CaTaO_3$ and $CaWO_3$ heavily overlap, enhancing the Wannier spreads of projected t_{2g} orbitals and reducing Hubbard U. Importantly, the d-d screening is reduced, allowing the remaining d-p screening to play a significant role in reducing V to U in both $5d^1$ and $5d^2$ configurations.

[1] P. Fazekas, *Lecture Notes on Electron Correlation and Magnetism* (World Scientific, Singapore, 1999), Vol. 5.
[2] N. F. Mott, Proc. R. Soc. A **62**, 416 (1949).
[3] F. Zhou, M. Cococcioni, C. A. Marianetti, D. Morgan, and G. Ceder, Phys. Rev. B **70**, 235121 (2004).
[4] A. I. Lichtenstein and M. I. Katsnelson, Phys. Rev. B **57**, 6884 (1998).
[5] O. Bengone, M. Alouani, P. Blöchl, and J. Hugel, Phys. Rev. B **62**, 16392 (2000).
[6] C. Loschen, J. Carrasco, K. M. Neyman, and F. Illas, Phys. Rev. B **75**, 035115 (2007).
[7] D. A. Andersson, S. I. Simak, B. Johansson, I. A. Abrikosov, and N. V. Skorodumova, Phys. Rev. B **75**, 035109 (2007).
[8] V. I. Anisimov, J. Zaanen, and O. K. Andersen, Phys. Rev. B **44**, 943 (1991).
[9] V. I. Anisimov, F. Aryasetiawan, and A. Lichtenstein, J. Phys.: Condens. Matter **9**, 767 (1997).
[10] K. Held, G. Keller, V. Eyert, D. Vollhardt, and V. I. Anisimov, Phys. Rev. Lett. **86**, 5345 (2001).
[11] A. I. Liechtenstein, V. I. Anisimov, and J. Zaanen, Phys. Rev. B **52**, R5467(R) (1995).
[12] B. J. Kim, H. Jin, S. J. Moon, J.-Y. Kim, B.-G. Park, C. S. Leem, J. Yu, T. W. Noh, C. Kim, S.-J. Oh, J.-H. Park, V. Durairaj, G. Cao, and E. Rotenberg, Phys. Rev. Lett. **101**, 076402 (2008).
[13] R. Arita, J. Kuneš, A. V. Kozhevnikov, A. G. Eguiluz, and M. Imada, Phys. Rev. Lett. **108**, 086403 (2012).
[14] P. Liu, S. Khmelevskyi, B. Kim, M. Marsman, D. Li, X.-Q. Chen, D. D. Sarma, G. Kresse, and C. Franchini, Phys. Rev. B **92**, 054428 (2015).
[15] P. A. Cox, *Transition Metal Oxides: An Introduction to their Electronic Structure and Properties* (Oxford University Press, New York, 2010).
[16] Y. Tokura and N. Nagaosa, Science **288**, 462 (2000).
[17] P. Hohenberg and W. Kohn, Phys. Rev. **136**, B864 (1964).
[18] R. O. Jones and O. Gunnarsson, Rev. Mod. Phys. **61**, 689 (1989).
[19] A. Georges, G. Kotliar, W. Krauth, and M. J. Rozenberg, Rev. Mod. Phys. **68**, 13 (1996).
[20] G. Kotliar and D. Vollhardt, Phys. Today **57**(3), 53 (2004).
[21] W. Metzner and D. Vollhardt, Phys. Rev. Lett. **62**, 324 (1989).
[22] K. Held, O. K. Andersen, M. Feldbacher, A. Yamasaki, and Y.-F. Yang, J. Phys.: Condens. Matter **20**, 064202 (2008).
[23] K. Held, Adv. Phys. **56**, 829 (2007).
[24] A. Toschi, A. A. Katanin, and K. Held, Phys. Rev. B **75**, 045118 (2007).
[25] G. Rohringer, H. Hafermann, A. Toschi, A. A. Katanin, A. E. Antipov, M. I. Katsnelson, A. I. Lichtenstein, A. N. Rubtsov, and K. Held, Rev. Mod. Phys. **90**, 025003 (2018).
[26] L. Boehnke, F. Nilsson, F. Aryasetiawan, and P. Werner, Phys. Rev. B **94**, 201106(R) (2016).
[27] T. Zhu and Garnet Kin-Lic Chan, Phys. Rev. X **11**, 021006 (2021).
[28] K. Held, C. Taranto, G. Rohringer, and A. Toschi, arXiv:1109.3972.
[29] J. Lee and K. Haule, Phys. Rev. B **95**, 155104 (2017).
[30] P. Sun and G. Kotliar, Phys. Rev. B **66**, 085120 (2002).
[31] S. Biermann, F. Aryasetiawan, and A. Georges, Phys. Rev. Lett. **90**, 086402 (2003).
[32] J. M. Tomczak, P. Liu, A. Toschi, G. Kresse, and K. Held, Eur. Phys. J.: Spec. Top. **226**, 2565 (2017).
[33] K. Haule and G. Kotliar, Phys. Rev. B **76**, 104509 (2007).
[34] A. I. Lichtenstein and M. I. Katsnelson, Phys. Rev. B **62**, R9283(R) (2000).
[35] K. Chahara, T. Ohno, M. Kasai, and Y. Kozono, Appl. Phys. Lett. **63**, 1990 (1993).
[36] S. Jin, T. H. Tiefel, M. McCormack, R. A. Fastnacht, R. Ramesh, and L. H. Chen, Science **264**, 413 (1994).
[37] Y. Shimakawa, Y. Kubo, and T. Manako, Nature (London) **379**, 53 (1996).

[38] S. Picozzi and C. Ederer, J. Phys.: Condens. Matter **21**, 303201 (2009).

[39] H. J. Zhao, W. Ren, Y. Yang, J. Íñiguez, X. M. Chen, and L. Bellaiche, Nat. Commun. **5**, 4021 (2014).

[40] J. Varignon, N. C. Bristowe, E. Bousquet, and P. Ghosez, Phys. Sci. Rev. **5**, 20190069 (2020).

[41] I. B. Bersuker and V. Polinger, Condens. Matter **5**, 68 (2020).

[42] I. B. Bersuker, Magnetochemistry **8**, 9 (2022).

[43] L. Chen, C. Setty, H. Hu, M. G. Vergniory, S. E. Grefe, L. Fischer, X. Yan, G. Eguchi, A. Prokofiev, S. Paschen, J. Cano, and Q. Si, Nat. Phys. **18**, 1341 (2022).

[44] V. Y. Irkhin and Y. N. Skryabin, J. Supercond. Novel Magn. **35**, 2141 (2022).

[45] B. Kim, P. Liu, and C. Franchini, Phys. Rev. B **95**, 115111 (2017).

[46] B. Kim, P. Liu, Z. Ergönenc, A. Toschi, S. Khmelevskyi, and C. Franchini, Phys. Rev. B **94**, 241113(R) (2016).

[47] H. Shinaoka, S. Hoshino, M. Troyer, and P. Werner, Phys. Rev. Lett. **115**, 156401 (2015).

[48] E. Pavarini, E. Koch, D. Vollhardt, and A. E. Lichtenstein, *The LDA+DMFT Approach to Strongly Correlated Materials: Lecture Notes of the Autumn School 2011, Hands-on LDA+DMFT; Autumn School Organized by the DFG Research Unit 1346 Dynamical Mean-Fiield Approach with Predictive Power for Strongly Correlated Materials at Forschungszentrum Jülich 4-7 October 2011* (Forschungszentrum, Zentralbibliothek, 2011).

[49] R. J. Bartlett, Annu. Rev. Phys. Chem. **32**, 359 (1981).

[50] F. Becca and S. Sorella, *Quantum Monte Carlo Approaches for Correlated Systems* (Cambridge University Press, Cambridge, 2017).

[51] V. I. Anisimov and O. Gunnarsson, Phys. Rev. B **43**, 7570 (1991).

[52] M. Cococcioni and S. de Gironcoli, Phys. Rev. B **71**, 035105 (2005).

[53] I. Timrov, N. Marzari, and M. Cococcioni, Comput. Phys. Commun. **279**, 108455 (2022).

[54] I. Timrov, N. Marzari, and M. Cococcioni, Phys. Rev. B **103**, 045141 (2021).

[55] G. C. Moore, M. K. Horton, E. Linscott, A. M. Ganose, M. Siron, D. D. O'Regan, and K. A. Persson, Phys. Rev. Mater. **8**, 014409 (2024).

[56] E. Antonides, E. C. Janse, and G. A. Sawatzky, Phys. Rev. B **15**, 1669 (1977).

[57] C. Franchini, R. Podloucky, J. Paier, M. Marsman, and G. Kresse, Phys. Rev. B **75**, 195128 (2007).

[58] G. K. H. Madsen, P. Blaha, K. Schwarz, E. Sjöstedt, and L. Nordström, Phys. Rev. B **64**, 195134 (2001).

[59] N. Marzari, A. A. Mostofi, J. R. Yates, I. Souza, and D. Vanderbilt, Rev. Mod. Phys. **84**, 1419 (2012).

[60] I. V. Solovyev and M. Imada, Phys. Rev. B **71**, 045103 (2005).

[61] K. Nawa, T. Akiyama, T. Ito, K. Nakamura, T. Oguchi, and M. Weinert, Phys. Rev. B **97**, 035117 (2018).

[62] R. Tesch and P. M. Kowalski, Phys. Rev. B **105**, 195153 (2022).

[63] M. S. Hybertsen, M. Schlüter, and N. E. Christensen, Phys. Rev. B **39**, 9028 (1989).

[64] T. Miyake and F. Aryasetiawan, Phys. Rev. B **77**, 085122 (2008).

[65] F. Aryasetiawan, M. Imada, A. Georges, G. Kotliar, S. Biermann, and A. I. Lichtenstein, Phys. Rev. B **70**, 195104 (2004).

[66] L. Vaugier, H. Jiang, and S. Biermann, Phys. Rev. B **86**, 165105 (2012).

[67] B. Amadon, T. Applencourt, and F. Bruneval, Phys. Rev. B **89**, 125110 (2014).

[68] E. Şaşıoğlu, C. Friedrich, and S. Blügel, Phys. Rev. B **83**, 121101(R) (2011).

[69] Y. Nomura, M. Kaltak, K. Nakamura, C. Taranto, S. Sakai, A. Toschi, R. Arita, K. Held, G. Kresse, and M. Imada, Phys. Rev. B **86**, 085117 (2012).

[70] B.-C. Shih, Y. Zhang, W. Zhang, and P. Zhang, Phys. Rev. B **85**, 045132 (2012).

[71] E. Şaşıoğlu, C. Friedrich, and S. Blügel, Phys. Rev. Lett. **109**, 146401 (2012).

[72] M. Kaltak, Merging GW with DMFT, Ph.D. thesis, University of Vienna, 2015.

[73] C.-N. Yeh and M. A. Morales, J. Chem. Theory Comput. **20**, 3184 (2024).

[74] F. Aryasetiawan, K. Karlsson, O. Jepsen, and U. Schönberger, Phys. Rev. B **74**, 125106 (2006).

[75] T. Miyake, F. Aryasetiawan, and M. Imada, Phys. Rev. B **80**, 155134 (2009).

[76] P. Liu, B. Kim, X.-Q. Chen, D. D. Sarma, G. Kresse, and C. Franchini, Phys. Rev. Mater. **2**, 075003 (2018).

[77] A. Hampel, P. Liu, C. Franchini, and C. Ederer, npj Quantum Mater. **4**, 5 (2019).

[78] D. Di Sante, B. Kim, W. Hanke, T. Wehling, C. Franchini, R. Thomale, and G. Sangiovanni, Phys. Rev. Res. **5**, L012008 (2023).

[79] P. Liu, M. Reticcioli, B. Kim, A. Continenza, G. Kresse, D. D. Sarma, X.-Q. Chen, and C. Franchini, Phys. Rev. B **94**, 195145 (2016).

[80] B. Kim, P. Liu, and C. Franchini, Phys. Rev. B **95**, 024406 (2017).

[81] B. Kim, K. Kim, and S. Kim, Phys. Rev. Mater. **5**, 035404 (2021).

[82] A. Hampel, J. Lee-Hand, A. Georges, and C. E. Dreyer, Phys. Rev. B **104**, 035102 (2021).

[83] J. Karp, A. Hampel, and A. J. Millis, Phys. Rev. B **103**, 195101 (2021).

[84] B.-L. Liu, Y.-C. Wang, Y. Liu, Y.-J. Xu, X. Chen, H.-Z. Song, Y. Bi, H.-F. Liu, and H.-F. Song, J. Chem. Phys. **158**, 084108 (2023).

[85] J. Souto-Casares, N. A. Spaldin, and C. Ederer, Phys. Rev. Res. **3**, 023027 (2021).

[86] A. Neroni, E. Şaşıoğlu, H. Hadipour, C. Friedrich, S. Blügel, I. Mertig, and M. Ležaić, Phys. Rev. B **100**, 115113 (2019).

[87] J.-B. Morée and B. Amadon, Phys. Rev. B **98**, 205101 (2018).

[88] C. Martins, M. Aichhorn, and S. Biermann, J. Phys.: Condens. Matter **29**, 263001 (2017).

[89] B.-C. Shih, T. A. Abtew, X. Yuan, W. Zhang, and P. Zhang, Phys. Rev. B **86**, 165124 (2012).

[90] S. K. Panda, H. Jiang, and S. Biermann, Phys. Rev. B **96**, 045137 (2017).

[91] E. G. C. P. van Loon, M. Rösner, M. I. Katsnelson, and T. O. Wehling, Phys. Rev. B **104**, 045134 (2021).

[92] C. Honerkamp, H. Shinaoka, F. F. Assaad, and P. Werner, Phys. Rev. B **98**, 235151 (2018).

[93] G. Kotliar, S. Y. Savrasov, K. Haule, V. S. Oudovenko, O. Parcollet, and C. A. Marianetti, Rev. Mod. Phys. **78**, 865 (2006).

[94] K. Held, I. A. Nekrasov, G. Keller, V. Eyert, N. Blümer, A. K. McMahan, R. T. Scalettar, T. Pruschke, V. I. Anisimov, and D. Vollhardt, Phys. Status Solidi B **243**, 2599 (2006).

[95] P. Liu and C. Franchini, Appl. Sci. **11**, 2527 (2021).

[96] D. Bohm and D. Pines, Phys. Rev. **82**, 625 (1951).

[97] D. Pines and D. Bohm, Phys. Rev. **85**, 338 (1952).

[98] D. Bohm and D. Pines, Phys. Rev. **92**, 609 (1953).

[99] M. Gell-Mann and K. A. Brueckner, Phys. Rev. **106**, 364 (1957).

[100] P. Nozières and D. Pines, Phys. Rev. **111**, 442 (1958).

[101] A. Kutepov, K. Haule, S. Y. Savrasov, and G. Kotliar, Phys. Rev. B **82**, 045105 (2010).

[102] S. Adler, Phys. Rev. **126**, 413 (1962).

[103] N. Wiser, Phys. Rev. **129**, 62 (1963).

[104] P. Liu, Low scaling GW method: Implementation and applications, Ph.D. thesis, Universität Wien, 2017.

[105] N. Marzari and D. Vanderbilt, Phys. Rev. B **56**, 12847 (1997).

[106] E. Şaşıoğlu, A. Schindlmayr, C. Friedrich, F. Freimuth, and S. Blügel, Phys. Rev. B **81**, 054434 (2010).

[107] A. A. Mostofi, J. R. Yates, Y.-S. Lee, I. Souza, D. Vanderbilt, and N. Marzari, Comput. Phys. Commun. **178**, 685 (2008).

[108] C. Franchini, R. Kovacik, M. Marsman, S. S. Murthy, J. He, C. Ederer, and G. Kresse, J. Phys.: Condens. Matter **24**, 235602 (2012).

[109] J. Kanamori, Prog. Theor. Phys. **30**, 275 (1963).

[110] G. Kresse and J. Hafner, Phys. Rev. B **47**, 558 (1993).

[111] G. Kresse and J. Furthmüller, Phys. Rev. B **54**, 11169 (1996).

[112] J. P. Perdew, K. Burke, and M. Ernzerhof, Phys. Rev. Lett. **77**, 3865 (1996).

[113] J. P. Perdew, A. Ruzsinszky, G. I. Csonka, O. A. Vydrov, G. E. Scuseria, L. A. Constantin, X. Zhou, and K. Burke, Phys. Rev. Lett. **100**, 136406 (2008).

[114] A. Nozaki, H. Yoshikawa, T. Wada, H. Yamauchi, and S. Tanaka, Phys. Rev. B **43**, 181 (1991).

[115] A. C. Komarek, T. Möller, M. Isobe, Y. Drees, H. Ulbrich, M. Azuma, M. T. Fernández-Díaz, A. Senyshyn, M. Hoelzel, G. André, Y. Ueda, M. Grüninger, and M. Braden, Phys. Rev. B **84**, 125114 (2011).

[116] H. Hannerz, G. Svensson, S. Y. Istomin, and O. D'yachenko, J. Solid State Chem. **147**, 421 (1999).

[117] F. Fukunaga and N. Tsuda, J. Phys. Soc. Jpn. **63**, 3798 (1994).

[118] L. Fruchter, V. Brouet, F. Brisset, H. Moutaabbid, and Y. Klein, CrystEngComm **21**, 3822 (2019).

[119] Y. S. Lee, J. S. Lee, T. W. Noh, D. Y. Byun, K. S. Yoo, K. Yamaura, and E. Takayama-Muromachi, Phys. Rev. B **67**, 113101 (2003).

[120] M. Ochi and K. Kuroki, Phys. Rev. B **99**, 155143 (2019).

[121] R. Mushkaev, F. Petocchi, V. Christiansson, and P. Werner, npj Comput. Mater. **10**, 182 (2024).

[122] J. Selisko, M. Amsler, C. Wever, Y. Kawashima, G. Samsonidze, R. U. Haq, F. Tacchino, I. Tavernelli, and T. Eckl, arXiv:2404.09527.

[123] F. Nilsson, L. Boehnke, P. Werner, and F. Aryasetiawan, Phys. Rev. Mater. **1**, 043803 (2017).

[124] A. Sekiyama, H. Fujiwara, S. Imada, S. Suga, H. Eisaki, S. I. Uchida, K. Takegahara, H. Harima, Y. Saitoh, I. A. Nekrasov, G. Keller, D. E. Kondakov, A. V. Kozhevnikov, T. Pruschke, K. Held, D. Vollhardt, and V. I. Anisimov, Phys. Rev. Lett. **93**, 156402 (2004).

[125] P. Wissgott, J. Kuneš, A. Toschi, and K. Held, Phys. Rev. B **85**, 205133 (2012).

[126] H. Park, A. J. Millis, and C. A. Marianetti, Phys. Rev. B **93**, 235109 (2016).

[127] L. Si, W. Xiao, J. Kaufmann, J. M. Tomczak, Y. Lu, Z. Zhong, and K. Held, Phys. Rev. Lett. **124**, 166402 (2020).

[128] J. M. Tomczak, M. Casula, T. Miyake, and S. Biermann, Phys. Rev. B **90**, 165138 (2014).

[129] A. Carta, A. Panda, and C. Ederer, Phys. Rev. Res. **6**, 023240 (2024).

[130] M. E. Merkel and C. Ederer, Phys. Rev. Res. **6**, 013230 (2024).

[131] I. R. Reddy, C.-J. Kang, S. Kim, and B. Kim, npj Comput. Mater. **10**, 286 (2024).

[132] F. Petocchi, F. Nilsson, F. Aryasetiawan, and P. Werner, Phys. Rev. Res. **2**, 013191 (2020).

[133] Z. V. Pchelkina, I. A. Nekrasov, T. Pruschke, A. Sekiyama, S. Suga, V. I. Anisimov, and D. Vollhardt, Phys. Rev. B **75**, 035122 (2007).

[134] O. E. Peil, M. Ferrero, and A. Georges, Phys. Rev. B **90**, 045128 (2014).

[135] M. Kinza and C. Honerkamp, Phys. Rev. B **92**, 045113 (2015).

[136] H. Shinaoka, M. Troyer, and P. Werner, Phys. Rev. B **91**, 245156 (2015).

[137] Q. Han, B. Chakrabarti, and K. Haule, arXiv:1810.06116.

[138] X.-J. Han, P. Werner, and C. Honerkamp, Phys. Rev. B **103**, 125130 (2021).

[139] C. J. C. Scott and G. H. Booth, Phys. Rev. Lett. **132**, 076401 (2024).

[140] C. Honerkamp, Phys. Rev. B **98**, 155132 (2018).

[141] A. van Roekeghem, T. Ayral, J. M. Tomczak, M. Casula, N. Xu, H. Ding, M. Ferrero, O. Parcollet, H. Jiang, and S. Biermann, Phys. Rev. Lett. **113**, 266403 (2014).

[142] M. Shishkin and G. Kresse, Phys. Rev. B **75**, 235102 (2007).

[143] G. P. Chen, V. K. Voora, M. M. Agee, S. G. Balasubramani, and F. Furche, Annu. Rev. Phys. Chem. **68**, 421 (2017).

[144] See NOMAD repository at DOI: 10.17172/NOMAD/2024.07.31-1.